REV.	BY & DATE	DESCRIPTION	CHECK	APPROVED & DATE
Prepared by Patrick Koehn	July 27, 2004	On-ground calibration report for the EPPS/FIPS instrument.		

ADVISORY: This document has NOT been reviewed for export control and therefore may be subject to ITAR regulations or requirements.

Ralph L. McNutt, Jr., Project Scientist — Date 8/5/04

Robert Gold, Payload Manager and Cognizant Co-Investigator — Date 8/5/04

Barry Mauk, Instrument Scientist — Date 7/29/04

Released — Date

Bruce Andrews, Instrument Engineer — Date 8/04/04

PART NUMBER	SIZE	NEXT ASSEMBLY	QTY./NA	USED ON	EFFECTIVITY - END ITEM SER. NO.	WEIGHT

THE JOHNS HOPKINS UNIVERSITY
APPLIED PHYSICS LABORATORY
11100 JOHNS HOPKINS ROAD, LAUREL, MARYLAND 20723-6099

MESSENGER Fast Imaging Plasma Spectrometer (EPPS/FIPS) Calibration Report

FSCM NO.	SIZE	DRAWING NO.	REV.
88898	A	7384-9472	A
SCALE NONE	DO NOT SCALE PRINT	SHEET 1 OF 42	

Table of Contents

ABSTRACT 3
INTRODUCTION 3
SCIENCE OBJECTIVES 4
Summary 4
Magnetospheric Ions 8
Pickup Ions 8
Solar Wind 8
INSTRUMENT REQUIREMENTS 9
Solar Wind 9
Magnetospheric Data 9
Pickup Ions 9
Design Considerations 10
INSTRUMENT DESCRIPTION 10
Instrument Summary 10
CALIBRATION FACILITY 12
Calibration Chamber 12
Subsystem Chamber 13
Ion Source and Diagnostics 14
UV Source and Diagnostics 14
Quantar Position-Sensing MCP System 15
Ionoptics Simulations 15
INSTRUMENT-LEVEL CALIBRATIONS 15
Overview 15
1. Calibration of the Electronics 16
2. Electrostatic Analyzer (ESA) 18
3. Efficiency 23
4. Mass Resolution 26
5. Rate vs. Rate Calibrations 27
6. In-flight Analysis Tools 31
7. UV Background Suppression 32
CALIBRATION SUMMARY 36
FIPS SCIENCE DATA PRODUCTS 36
Mass and Energy Spectra 36
Proton Velocity Distribution Functions 38
Heavy Ion Velocity Distribution Functions 38
PHA Events 39
Rate Counters 39
REFERENCES 40

ABSTRACT

The Fast Imaging Plasma Spectrometer (FIPS) is an imaging mass spectrometer, and is part of the Energetic Particle and Plasma Spectrometer (EPPS). EPPS is on NASA's MESSENGER mission, the first Mercury orbiter. FIPS has a very small footprint and its mass is much less than that of other comparable instruments. It maintains a nearly full-hemisphere field of view with a novel electrostatic analyzer system, which is then combined with a position sensitive time-of-flight system. The data processing and compression is done as part of the Energetic Particle Spectrometer (EPS), which is also part of EPPS. Here, we discuss the calibration of the FIPS sensor head. EPS is covered in a different calibration report.

INTRODUCTION

FIPS, together with EPS, is part of the EPPS instrument dedicated to analyze Mercury's space environment. For protons FIPS and EPS have overlapping energy ranges covering over four decades in energy. FIPS and EPS have separate mechanical spacecraft interfaces, but have common data and electrical spacecraft interfaces. The event processing unit (EPU) is collocated with the EPS sensor. FIPS is therefore a passive sensor that is commanded from the EPU electronics board. It is important to note that there is a limitation to this calibration report. Ideally, all calibrations would be performed using this EPU interface. However, the delivered software and final EPU interface were not available for these calibrations. The calibrations were performed using an EPU simulator and calibration software to ensure timely delivery. Post-delivery calibrations were performed at the Applied Physics Laboratory (APL) using a FIPS simulator and EPS data.

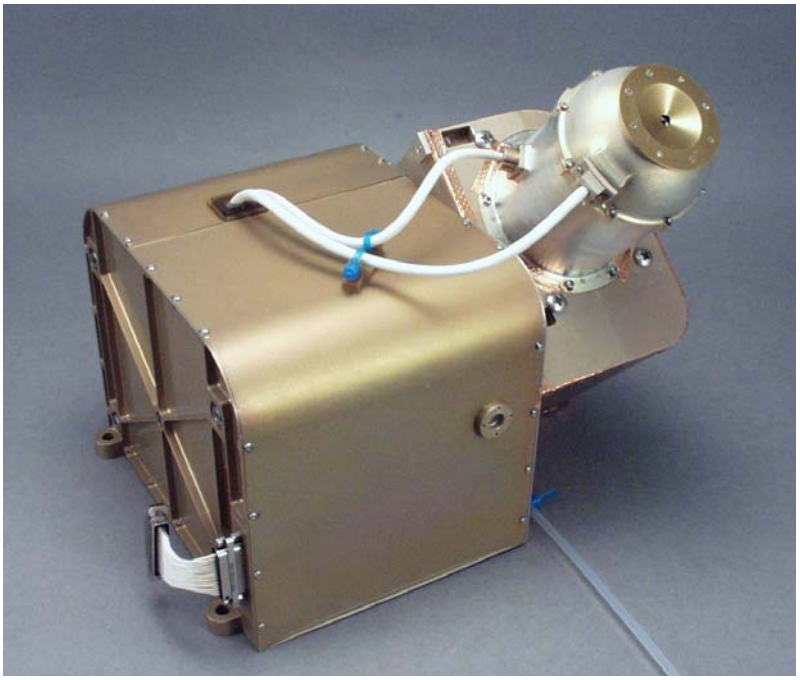

Figure 1. An image of the calibrated FIPS sensor before it was delivery to EPPS in May 2003.

FIPS is a completely new instrument, designed for the MESSENGER mission to Mercury [Gloeckler, *personal communication*, 1994; Zurbuchen et al., 1998; Koehn, 2002]. A photograph of the instrument

is shown in Figure 1. It is designed to characterize ionized species in a range of energy-per-charge (E/q) from as low as 50 eV/q up to 20 keV/q. One of the innovations in this sensor is a new electrostatic analyzer (ESA) system geometry that enables a large instantaneous (~1.5π) field of view. Particles which pass through the ESA have a known E/q, proportional to the stepped deflection voltage. They are then post-accelerated by a fixed voltage, before passing thought a very thin carbon foil. The ions travel a known distance and hit the stop micro-channel plate (MCP), while forward-scattered electrons from the carbon foil are focused onto the start MCP. Position sensing with a wedge-and-strip anode in the start MCP assembly determines the initial incidence angle. The mass-per-charge (M/q) of a given ion follows from the known E/q and the measured the time of travel, τ, allowing reconstruction of distribution functions for different M/q species. In its NORMAL (nominal) scan mode, the ESA system covers the E/q range in 64 logarithmically spaced steps every 65 seconds. It can also run in a fast "BURST mode" that allows highly focused sweeps within only 2 seconds.

SCIENCE OBJECTIVES

Summary

During its rapid flybys Mariner 10 imaged ~45% of Mercury's surface. Figure 2 shows an image taken by Mariner during one of its flybys. When looking at this data in detail, the surface of Mercury appears to be divided into four major terrains: heavily cratered regions, intercrater plains, hilly and lineated terrain, and smooth plains. The differentiation between the oldest, heavily cratered regions and the very smooth plains provide important information about a possible volcanic history of Mercury. However, both, surface composition information and detailed mapping of the other ~55% are needed to make firm conclusions about this.

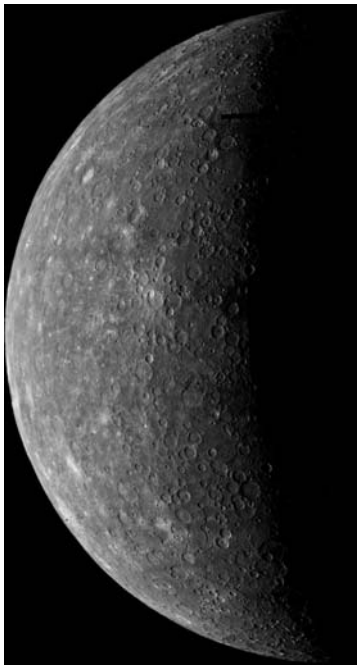

Figure 2 - Mariner image of Mercury surface showing areas with highly variable crater density. (Image courtesy JPL)

One surprise from the Mariner 10 flybys was the discovery of a substantial internal magnetic field in planet Mercury [Ness et al., 1974, 1975]. The magnetic dipole moment is likely perpendicular to the ecliptic, aligned with the Mercury's rotation axis. The exact size of the dipole moment is still under discussion and strongly depends on the assumptions on higher order moments of the magnetic field distribution. The most commonly cited dipole moment is 300 nT R_M^3. The accuracy of this number is subject to limitations imposed by the Mariner 10 encounter trajectories. However, the observed field magnitude in Mercury's environment is large enough to conclude with certainty that there are significant internal (as opposed to vestigal, as on Mars) magnetic field contributions, and that the observed magnetic field cannot be explained solely as a result of planet-solar wind interactions. The presence of this magnetic field therefore dominates the space environment of the planet.

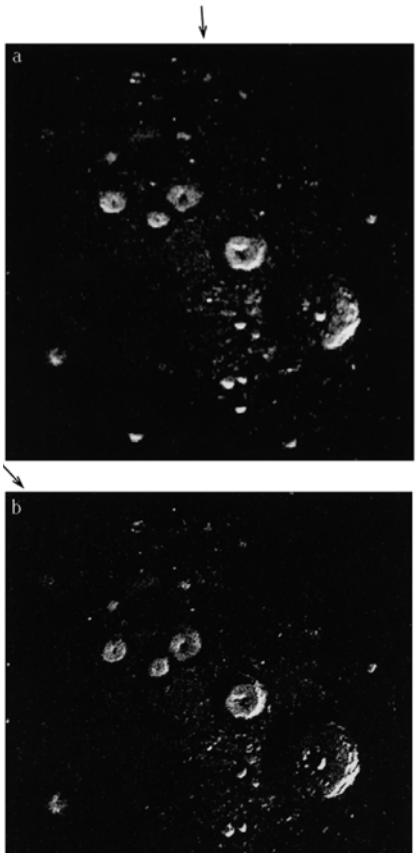

Figure 3 - Polar deposits observed by ground-based radar. These highly reflective materials are widely thought to consist of water-ice, but may be associated with Sulfur deposits. From [Harmon et al., 2001]

One very crucial observation of the post-Mariner era is the observation of radar-reflective materials at Mercury's poles [Slade et al., 1992]. Figure 3 shows such observations from Harmon et al., (2001). The reflective materials are only found in many craters close to Mercury's polar regions. The high polarization ratios observed from these regions are similar to those of icy satellites of the outer planets. Therefore these reflecting areas are widely thought to be caused by water ice. Because of the near zero obliquity, there are permanently shadowed craters in the polar regions. Also, this dynamic configuration is sufficiently stable that the ice in these craters may survive for many millions of years [Vasavada et al., 1999]. Sprague et al. (1995) proposed an alternative hypothesis that the polar deposits are composed of

elemental sulfur. The shaded craters act as cold-traps for volatile species and may have trapped S emitted from Mercury's surface and re-deposited in a neutral or ionized state. This process will be discussed in more detail in a later section.

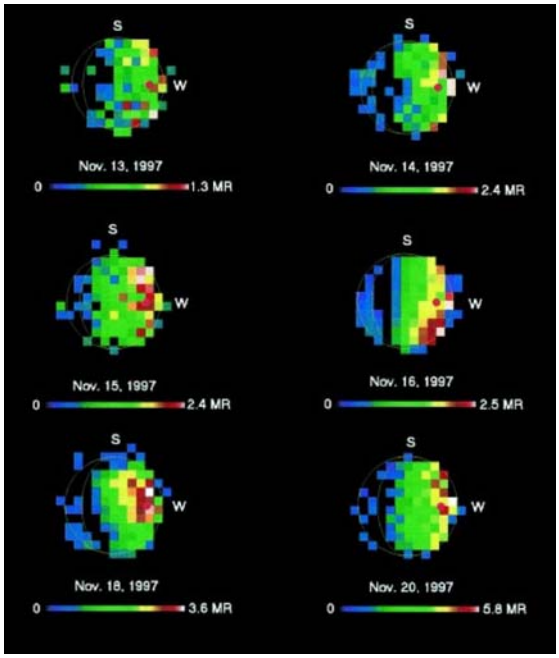

Figure 4 - Intermittent Na event discussed by Potter et al. (1999). These events may be closely associated with solar wind - planet interactions.

Any discussion of S in Mercury's vicinity should be performed in the context of the overall sources and sinks of volatile species in Mercury's environment. Mercury's atmosphere is completely exospheric, and is known to have a surface-density of roughly 10^4 atoms/cm^3, mostly consisting of H, He, O, Na, and K [Hunten et al., 1988]. Here, the H and He abundance measurements come from Mariner airglow spectrometer data [Broadfoot et al., 1976], whereas Na and K come from remote observations [Potter and Morgan, 1985, 1986]. Calcium has also been detected in the atmosphere [Bida et al., 2000]. The Na density is observed to be highly variable in space and time (Figure 4). These changes appear to be associated with solar radiation changes [Potter and Morgan, 1987; Ip, 1990], but may also be a direct result of magnetosphere-planet interactions [Koehn, 2002]. In general, only a comprehensive inventory of atomic species in Mercury's environment, taken by in situ measurements, will provide important clues about planetary and solar wind sources of the tenuous exosphere associated with Mercury.

The FIPS instrument is one half of the Energetic Particle and Plasma Spectrometer instrument suite. The science measurement objectives of the EPPS instrument suite are to:

- Provide the capability to distinguish between solar and planetary sources of magnetospheric species.
- Provide in situ detection of H^+ or S^+ enrichment over polar regions.
- Provide the composition of magnetospheric ions and pickup ions in the solar wind from sputtered neutrals.

FIPS shall be capable of measuring and analyzing the elemental species H, ^{3}He, ^{4}He, O, Ne, Na, K, S, and Ar over an energy/charge range between 50 eV to 20 keV. In this energy range there are three major plasma sources: the Mercury magnetosphere, Mercury pickup ions and the solar wind.

Most of the **Mercury magnetospheric ions** presumably are from the solar wind. These particles have never been observed before. These measurements here are therefore exploratory. Due to the relatively small magnetic field of Mercury, and the lack of a stationary atmosphere/ionosphere system, the source of magnetospheric ions are therefore directly from the solar wind.

These magnetospheric ions should be distinguished from neutral species sputtered into the exosphere of Mercury. These particles are ionized within hours and then produce **Mercury pickup ions**. These ions have also not been observed, but can be inferred from remote neutral observations from Mariner and the Earth. Their density is likely much smaller than the average magnetosphere density.

Finally, the entire system is being driven by the **solar wind**. This is the best known particle source in the inner heliosphere, based on Helios data at the same heliocentric radius as Mercury [Schwenn, 1990]. The solar wind is highly supersonic, even in the inner heliosphere. Most of the solar wind is shielded from FIPS based on thermal considerations, and will not be observed in general. However, solar wind will be an important particle source for calibration during MESSENGER's transit to Mercury.

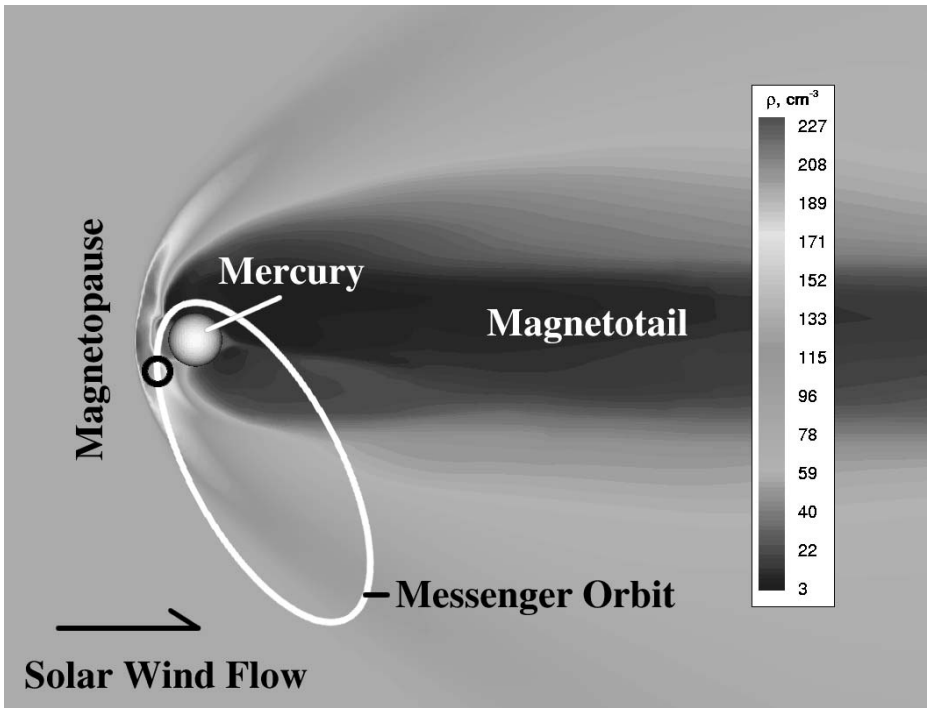

Figure 5 - The structure of Mercury's magnetosphere with superposed MESSENGER orbit. During its orbit FIPS will measure solar wind, Mercury's bow shock and magnetosheath, as well as magnetospheric components. Marked with a black circle is a time in orbit at which MESSENGER crosses from closed fields into cusp fields with direct access to the polar regions of Mercury. In these polar regions, we expect a major source of pickup ions that is accelerated by the convective field of the magnetospheric plasma. [Koehn, 2002]

Magnetospheric Ions

The expected magnetospheric particle population is expected to be highly variable and highly dependent on the location of MESSENGER around Mercury. This is now illustrated using three-dimensional MHD calculations of the Mercury environment by Kabin et al. (2000). In that simulation, particles are flowing into the planet, but the planet does not provide a source of particles. The typical spatial scales of the magnetosphere are shown in Figure 5. The simulations shown in Figure 5 assume that Mercury is an insulator. This is likely not the case and induction currents inside of Mercury may play an important role.

On the dayside FIPS will concentrate on the solar wind interaction with the Mercury magnetosphere. The location and structure of the bow-shock and the magnetopause will be of interest. On the nightside, FIPS will concentrate on the structure of the magnetosphere, particularly, the transient phenomena associated with the reconnection of magnetic flux.

Pickup Ions

Pickup ions are Mercury ions – and also solar wind ions - that are emitted in a neutral state and subsequently ionized in the Mercury environment. These ions provide direct information about the composition of Mercury's crust and exosphere. The masses of these ions are likely between those of H and Ar.

The typical fluxes of these pickup ions can be estimated using neutral particle observations. Pickup ions are being generated by ionization from these neutrals. The pickup ion fluxes are likely spatially dependent. The mass resolution of the instrument has to be sufficient to separate these components, particularly being able to separate C, N, and O, which results in a mass resolution of $\Delta M/M$ ~5%.

Solar Wind

The properties of the solar wind in the Mercury orbit are well understood based on plasma and field measurements of the NASA-DARA mission Helios that involved two spacecraft on highly elliptical orbits with a perihelion around 0.3 AU. (See http://www.linmpi.mpg.de/english/projekte/helios/). The major properties are summarized in Table 1. The solar wind was observed to occur in two distinctly separate dynamic states and are therefore treated separately. All parameters are given with their value at 1 AU, together with their scaling with R, the heliocentric radius.

Table 1. Expected behavior of heliospheric plasmas throughout the MESSENGER transit to Mercury and the Mercury orbit. R indicates the heliospheric distance in units of 1 AU.

Parameter	Slow	Fast
Speed [km/s]. R^0	348	667
Density [/cc]. R^{-2}	10.2	3.0
Kinetic temperature [10^3 K] . R^{-1}	55	280

INSTRUMENT REQUIREMENTS

Table 2. Science Requirements. These science requirements are consistent with the original FIPS proposal. They are quantified based on previous observations in the heliosphere, model calculations such as the one shown in Figure 5, and model calculations such as described by Zurbuchen et al. (2004).

Measurement	Feature	Range	Resolution
Magnetospheric Plasma	Density [/cc]	100	20%
	Velocity [km/s]	50-800	5%
	Particle flux [$cm^{-2}s^{-1}$]	10^{5}-10^{12}	10%
	Temperature [eV]	50 –1000	20%
	Mass/charge	M/Q = 1, 5	20%
Pickup Ions	Density [/cc]	0.1	20%
	Velocity [km/s]	1-1000	10%
	Particle flux [$cm^{-2}s^{-1}$]	$<10^{5}$	20%
	Mass/Charge	1-30	6% for C,N, O
Solar Wind	Density [/cc]	50-200	N/A
	Velocity [km/s]	400-700	N/A
	Particle flux [$cm^{-2}s^{-1}$]	10^{9}-10^{11}	N/A
	Temperature [eV]	50	N/A
	Mass/charge	1-5	6%

Some resolution requirements given in Table 2 deserve further discussion.

Solar Wind:

A programmatic decision was made by MESSENGER not to pursue solar wind measurements. No resolution requirement is therefore derived from this. The only resolution requirement relative to solar wind data allows distinguishing solar wind protons and alpha particles, as well as average Fe charge states. This will allow a characterization of the solar wind, even if the large majority of solar wind particles cannot enter FIPS. Under certain circumstances, such as specific spacecraft position, and deflection of the solar wind out of the radial direction, the solar wind bulk flow is expected to be detected by FIPS.

Magnetospheric Data:

The lack of an ion deflector precludes a determination of magnetospheric density, velocity and temperature under all conditions. The magnetospheric plasma detection will be most effective in low Mach-number plasmas and when the plasma flow vector is deflected substantially out of the solar direction. This is always the case close to perihelion, and often in the downwind direction.
There is a science driven requirement for fast measurements of magnetospheric plasma of less than 10s.

Pickup Ions:

The fluxes of pickup ions are derived under the assumption of a given neutral density and known ionization rates. Absolute densities and density distributions are not known.

Design Considerations
The following requirements and constraints most affected the design of the FIPS sensor.

- Minimize mass, volume, and power (final mass, volume and power: 1.41 kg , 17.0 x 20.5 x 18.8 cm^3 <2.0 watts).
- UV suppression to permit operation in full sunlight near Mercury
- Wide field-of-view needed for three-axis-stabilized spacecraft.
- Wide event-rate dynamic range
- Mass resolution
- High voltages are required for the electrostatic analyzer, and for post-acceleration, which enables low energy ions to penetrate the Carbon foil. The constraints on size and mass were a significant driver for the high voltage design.
- Energy-per-charge dynamic range, fast transitions between steps
- Fast time-resolution capability
- Low bit rate
- Instrument control, such as the scanning of the electrostatic analyzer deflection voltage is performed by EPPS software.
- Event data is transferred at high speed to EPS, where the data volume is reduced and telemetry data packets are formatted by a shared EPPS event processing board.

The design of the FIPS instrument and the executed calibration plan are consistent with all these requirements and constraints.

INSTRUMENT DESCRIPTION

FIPS is composed of three major subsystems: an electrostatic analyzer (ESA) system, a time-of-flight (TOF) system, and the sensor electronics. Figure 6 illustrates the FIPS sensor in cross section.

The ESA serves both as a UV trap and an energy-per-charge filter, allowing only ions of a very specific energy-per-charge interval (determined by a stepped deflection voltage) to pass through the system. Ions enter through a small annular aperture, seen on the left side of Figure 3. Within this aperture there is a set of 24 radial openings that the ions must pass through. These slots limit ions to a small band along the symmetry axis of the ESA, in both position and velocity, eliminating ions that might spiral within the cylindrically symmetric ESA. The ions then enter a region where their trajectories are curved by the electrostatic field between the positive outer deflection plate and the grounded inner cylinder and field shaping fins. Ions must then pass through the collimator. Its openings, an array of small circular arcs, are aligned with the axis of symmetry of the ESA so that ions that are not traveling parallel to the axis are eliminated. The E/q resolution and geometric factor of the ESA are determined by the angular acceptance of the collimator, the area of its openings, and the size of the entrance aperture. After ions have passed through the first deflection region and first collimator, the ESA has performed its purpose as an E/q filter. However, at this point UV attenuation is not sufficient, so an hourglass shaped deflection region between the first and second collimators has been added to provide the needed UV suppression.

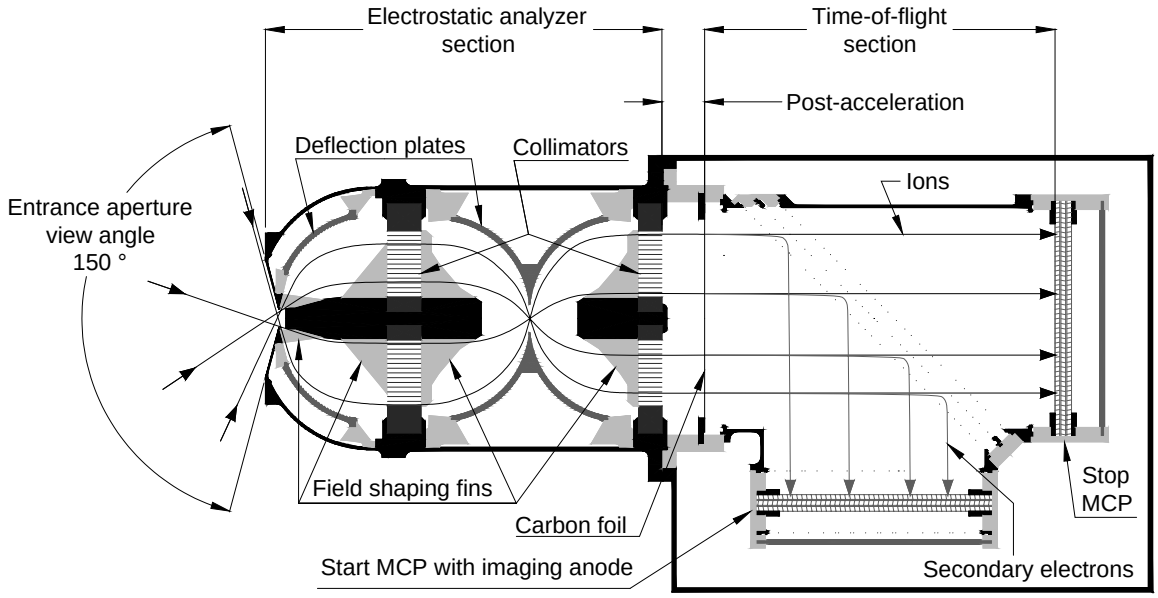

Figure 6. Cross section of the FIPS functionality. For details refer to text.

Ions are post-accelerated by a potential drop of up to -15 kV just before entering the TOF section. The energy they gain enables the lowest energy ions to pass through the carbon foil (and reduces energy straggling for all ions).

The TOF system is a typical 'mirror-harp' design that relies on wire harps to establish potential regions, yet allows particles to pass between the wires. The speed of an ion is determined by measuring its travel time between the carbon foil and the stop MCP, separated by a distance of 7.45 cm. As an ion passes through the carbon foil, it loses a small amount of energy (ε), is subjected to some directional scattering as a result of interactions with the foil, and emerges with a charge state that is predominantly neutral or singly charged. Low energy secondary electrons are also released from the foil, due to ion scattering interactions. These secondary electrons are accelerated, and then reflected by the diagonal mirror harp onto the start MCP, which produces a start signal. After leaving the foil, the ion travels straight through the TOF system until it strikes the second MCP, which produces a stop signal. The time difference between the start and stop signals is measured by the electronics. The time-of-flight of the ion is known once a correction is made for the travel time of secondary electron from foil to start MCP (a fixed offset – typically five nanoseconds, depending on potentials within the TOF system).

In addition to E/q filtering and TOF measurement, FIPS measures the direction an ion came from (it is an imaging spectrometer). Within the cylindrically symmetric ESA, an ion's trajectory is curved toward the axis by the electric field, until it is normal to the surface of the collimator. The azimuth angle of the incoming ion is not changed by the ESA. Radial fins every 15 degrees prevent ions from spiraling within the ESA (these fins are also used for field shaping of the ion optics). The greater the polar angle (the angle between the direction of the incident ion and the symmetry axis of the ESA) the greater the

radial position of the ion where it passes through the collimator. The TOF system has a circular cross section, with the same axis of symmetry as the ESA. Ions that exit the collimator are moving parallel to this axis, so their location on the carbon foil is the same as in the collimator. The electron optics of the TOF system maps the position of the secondary electrons that are released from the carbon foil onto the start MCP (in a mirror image). A wedge-strip-zigzag (WSZ) anode behind this MCP allows two-dimensional position sensing of the event on the MCP. In summary, the position information recorded by the time-of-flight system can be mapped back to the ion's angle of entry into the ESA.

The FIPS electronics consists of five board-level subsystems packaged with the sensor: 1) The 'Digital' board includes fast-pulse amplifiers, constant-fraction timing discriminators, and a time-to-digital converter in order to measure time-of-flight. It also includes an FPGA that handles instrument control and takes some of the load off the shared event processor housed in EPS, and the interface electronics. 2) The 'Analog' board contains three channels of pulse shaping electronics to measure position from the WSZ anode. A single analog-to-digital converter (ADC) is used in conjunction with an analog multiplexer to digitize the amplitude of these pulses, and to measure various housekeeping parameters. A precision digital-to-analog converter (DAC) sets the ESA deflection voltage. 3) The deflection system high voltage power supply provides the voltage for the ESA. Its output covers the range from +35 to +15000 volts, and it is designed to transition rapidly between output levels. 4) The post-acceleration power supply provides an output voltage up to -15 kV for the TOF system. 5) The MCP bias power supply supplies both MCP assemblies with several output voltage taps for each. Its highest output voltage is -3600 volts.

Instrument Summary

Table 3 - Summary of FIPS characteristics

Characteristic	Value
Mass	1.41 kg
Volume	17.0 x 20.5 x 18.8 cm^3
Power (average/maximum)	1.9/2.1 W
Bitrate (avg)	80 bps
Field of View	1.4π
Energy range	50 eV – 20 keV
M/Q range	1 – 40 amu/e
Scan Speed (nominal/burst)	65/2 sec

CALIBRATION FACILITY

Calibration Chamber

The tests were performed at the University of Michigan Space Physics Research Laboratory using the "Calibration Chamber." This chamber is ideally suited to the tasks of full-instrument and subsystem testing. The vacuum chamber is a freestanding unit, 26" diameter, and has a volume of over 20000 cubic inches (see Fig. 7). This is more than adequate for the testing of small to moderately-sized devices. The system is pumped down to a nominal vacuum with a mechanical roughing pump, and then the pressure

is reduced to the millitorr level by two LN2-cooled sorption pumps. A CTI-Cryogenics cryopump is then used to achieve the system's operating vacuum of 10^{-7} Torr. It is also equipped with an independent compressed air supply for valve operation. The system is equipped an electron collision ion source with mass-selector and beam diagnostic. The beam shaping occurs behind a 1-m drift tube to allow for beam cooling and collimation, as well as post-acceleration up to 20-kV. A voltage break allows the beam source and drift tube to be floated to high voltages. Beam diagnostic and instrument can be mounted on a manipulator with full 4D electronic control. Finally, the perimeter of the system has a number of ports of various sizes, a residual gas analyzer port, and numerous BNC, SHV, and Bendix feedthroughs for prototype control and data collection. One of these ports has been used to do the UV calibrations and tests described below.

This chamber and other facilities, such as ion sources, power supplies, Faraday cups, Wien filter, Residual Gas Analyzer (RGA), etc., were available full-time during the entire test schedule of FIPS.

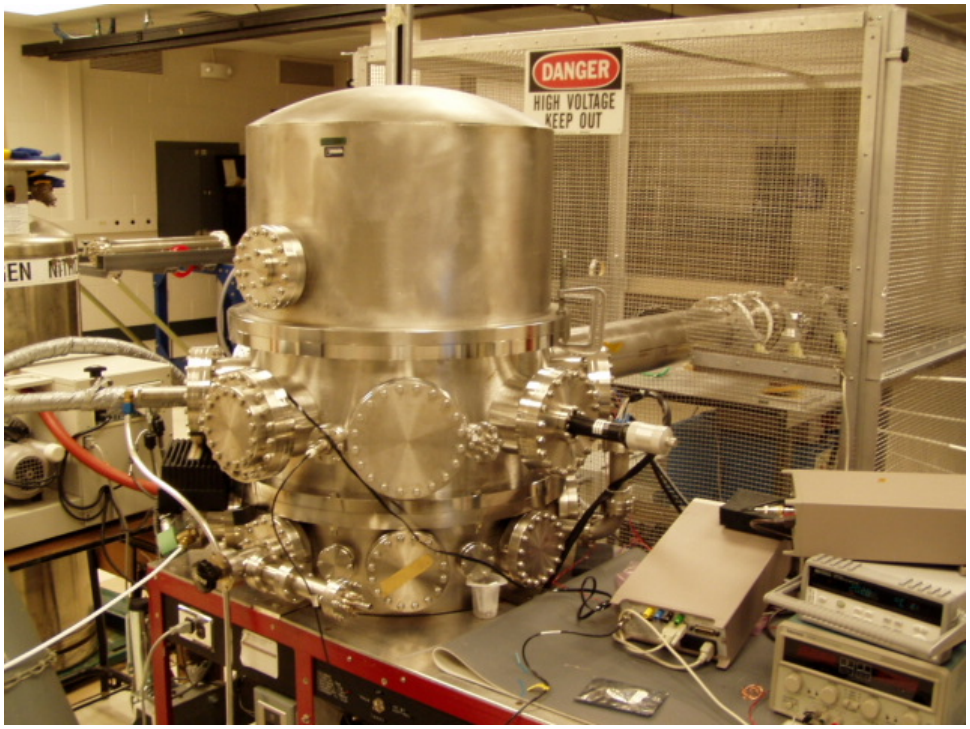

Figure 7. Calibration chamber. This calibration system was developed for the FIPS final calibrations.

Subsystem Chamber

Additional tests were performed in another room using the "Subsystem Chamber" (Figure 8). This system was designed for use as part of a calibration facility, possessing an array of motion control systems. It is a freestanding unit, with a volume of more than 9000 cubic inches. This relatively small chamber is more than adequate for the precision testing of small-sized devices. The system is evacuated to low vacuum by a scrollpump, and then further reduced to the millitorr range by a turbopump. A final vacuum of 1×10^{-7} Torr is achieved through the use of a CTI Cryogenics cryopump. The system is

equipped with an ion source comparable to the one on the calibration system, a 1-m drift tube for beam cooling and collimation, and a 20-kV voltage break, allowing the beam source and drift tube to be floated to high voltages. Finally, the perimeter of the system has a number of ports of various sizes, and numerous BNC and SHV feedthroughs for instrument control and data collection. A set of three vacuum-proof motors is available to articulate FIPS through its entire field of view. These motors are computer controlled and allow accurate positioning to within 0.1°.

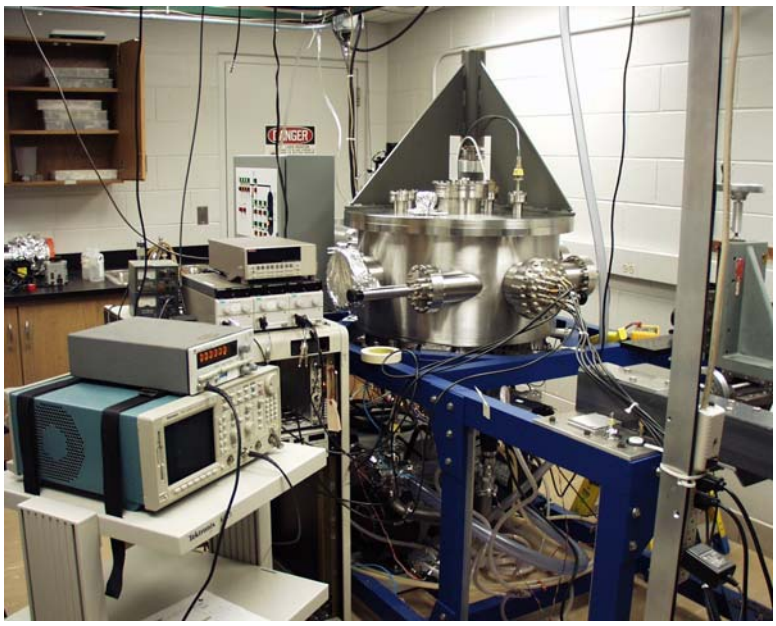

Figure 8. Subsystem chamber. This system was used for calibration and test of FIPS subsystems.

Ion Source and Diagnostics

We use identical ion sources in both vacuum systems. The ion source is a standard electron collision source with variable extraction voltage up to 7-keV particle energy internal to the source. Subsystem tests of the electrostatic analyzer and the time-of-flight system rely only on this primary voltage. For final calibration, the ion beam is mass-selected using a Wien filter, before it is accelerated by an external voltage. In this configuration, the particle energy is up to 30 keV.

The primary beam is monitored using a combination of a Faraday cup and an MCP. The Faraday cup is used for the measurement of the absolute current, but only works at large enough current (or, high counting rate) for sufficient accuracy. The MCP, however, has an upper limit for the counting rate. In the range where these two devices overlap, the MCP can be inter-calibrated to absolute values. The MCP can then be used at lower counting rates to monitor the primary ion beam to less than 5% accuracy. This process is routinely used in calibration chambers for ion instruments in the FIPS energy range.

UV Source and Diagnostics

The UV source used is a resonance line source from the Opthos Company. This line source is an electrode less lamp filled with hydrogen at a pressure of about 1 Torr to emit light in the Lyman-alpha range. This lamp is made according to the general design of Okabe with an output of 3.0×10^{14}

photons/sec. UV light is transmitted through a magnesium fluoride window on the lamp, which is inserted into a vacuum chamber feed through. The lamp operates by using a microwave source to generate discharges in the gas. The flux was measured using a calibrated UV-sensitive photodiode.

Quantar Position-Sensing MCP System

The calibration of the ion-optics systems often relied on a position-sensitive detector from Quantar Technologies, Inc. This device is a chevron stack of MCPs backed by a resistive anode. Charged particles impact the MCP, creating a cascade of electrons that are driven back to the anode, where they are detected. The position of the centroid of the electron cloud is calculated in the Quantar Electronics package. It is an effective tool for beam diagnostics and is especially useful for the testing of prototype electrostatic analyzers, or any system in which position sensing of a charged particle beam is necessary.

Ionoptics Simulations

The goal of these simulations was to provide an estimate of the four important performance parameters of this instrument: energy resolution, analyzer constant, angular resolution and effective aperture. We chose the simulation software package SimIon as our simulation programming environment. It provided the best flexibility and speed for our needs. It is a relatively simple program. The simulation geometry is constructed using either a graphical interface or a programming structure unique to the ray-tracing program. The geometry is laid out in gridpoints, and each gridpoint is assigned a voltage. The program then solves Laplace's equation for the potentials and fields between the simulated electrodes. Simulated ions may then be introduced to the system and their trajectories tracked and recorded for later analysis.

The simulated geometry was of sufficient resolution to model all the important features of the entrance system. An ion-optical system of the FIPS ESA's complexity requires a great deal of computing power to be represented accurately in a simulation environment, so efforts were made to utilize the ESA's symmetry wherever possible. The minimum resolution in the simulation was 5 grid points per millimeter. Transmitted ion trajectories are far enough from any electrode surface that they will be unaffected by any field irregularities introduced by this relatively low resolution. A large portion of the system was created by rotating a 10 gridpoints/mm 2D frame around the central axis of symmetry, further decreasing the computer system requirements. A virtual ion traveling through this rotated frame will “see” a three-dimensional geometry and field, so this approximation is acceptable. The collimator plates are rendered at an even higher resolution (20 gridpoints/mm), and are used as beam stops within field free regions of the simulation held at ground potential. The simulated collimator plate slits are identical to the collimators installed in the prototype, as are the finlike azimuthal collimators. Each transmitted ion's initial and final energy, direction and position were stored for analysis, and the information was used to generate estimates of the instrument's performance characteristics.

INSTRUMENT-LEVEL CALIBRATIONS

Overview

The instrument-level calibrations fall in six distinct and complementary parts. All these parts directly affect the instrument performance. They form a complete set of calibrations, with one caveat already mentioned above, namely, that the flight software was not used for the system-level calibrations.

These calibrations include

1. **Electronics Calibration:** This falls in two parts. First, the time-of-flight electronics has to be calibrated to provide absolute sensitivity. This affects both speed (V) and mass per charge (M/Q) measurements in the device. Second, the analog circuit has to be calibrated. This calibration affects the position sensing and hence angular resolution of the program.
2. **Electrostatic Analyzer (ESA):** This is a set of end-to-end tests of the electrostatic system. The instrument performance is judged by comparisons with simulation results. This affects the total geometric factor (or, sensitivity) and range and resolution in energy per charge (E/Q) and angular range and resolution.
3. **System Efficiency:** This is from end-to-end tests of the entire sensor, including flight electronics. The results of these calibrations are test-cases of mass-dependent efficiencies, as well as efficiency dependent on particle incidence direction.
4. **Mass resolution:** Finally, a combination of test 1-3, the mass resolution can be evaluated using the usual process.
5. **Rate vs. Rate and Proton** rejection test: The FIPS instrument is tested to characterize its processing capabilities as a function of increasing input flux, and the proton rejection function of the instrument is tested.
6. **In flight analysis tools:** There are a number of electronic tools that will allow in-flight testing of the FIPS instrument. These in-flight calibration tools were calibrated. They include a test-pulser designed to calibrate the position-sensing function of the instrument.
7. **Background suppression**: There are two aspects to this measurement. First, the instrument's ESA has to suppress UV photons which can lead to spurious background. Second, secondary electron emission from electrostatic mirrors can also produce such background.

1. Calibration of the Electronics

Some measurements that are needed to understand the internal operation of the instrument and interpret the higher level calibrations can only be done at the subsystem level. Among these is the time calibration of the TOF electronics. The purpose of this test was to calibrate the electronics functions and define the translation of digital channel number to actual signal-strength. These calibrations were directly included in on-ground data processing software.

The FIPS TOF electronics time calibration was done using laboratory equipment. Start and stop test signals came from an Agilent 81130A pulse generator with pulse delay accuracy of 0.001% ± 100 ps. The instrument TOF time standard is derived from a 12 MHz clock signal from EPS. For this test a prototype EPS unit supplied the clock signal, but this is not expected to affect the results.

The time-to-digital converter measurement data, along with a linear fit to the data are plotted in Figure 9. The maximum TOF that can be measured is 662 ns, corresponding to a maximum raw TOF output of 2047. For events with TOF longer than this, the valid event flag is not set. For zero delay the raw TOF output is 1. Although the CFD timing discriminators have adjustable levels, during calibration they were at fixed levels. The start discriminator was set to level 84 (hex), corresponding to 33.5 mV, or 0.72 pico-coulomb. The stop discriminator was set to level 89 (hex), corresponding to 31 mV, or 0.68 pico-coulomb. Housekeeping readouts of pulse-height measurements for the wedge, strip, and zigzag signals can be used to monitor the start-MCP gain.

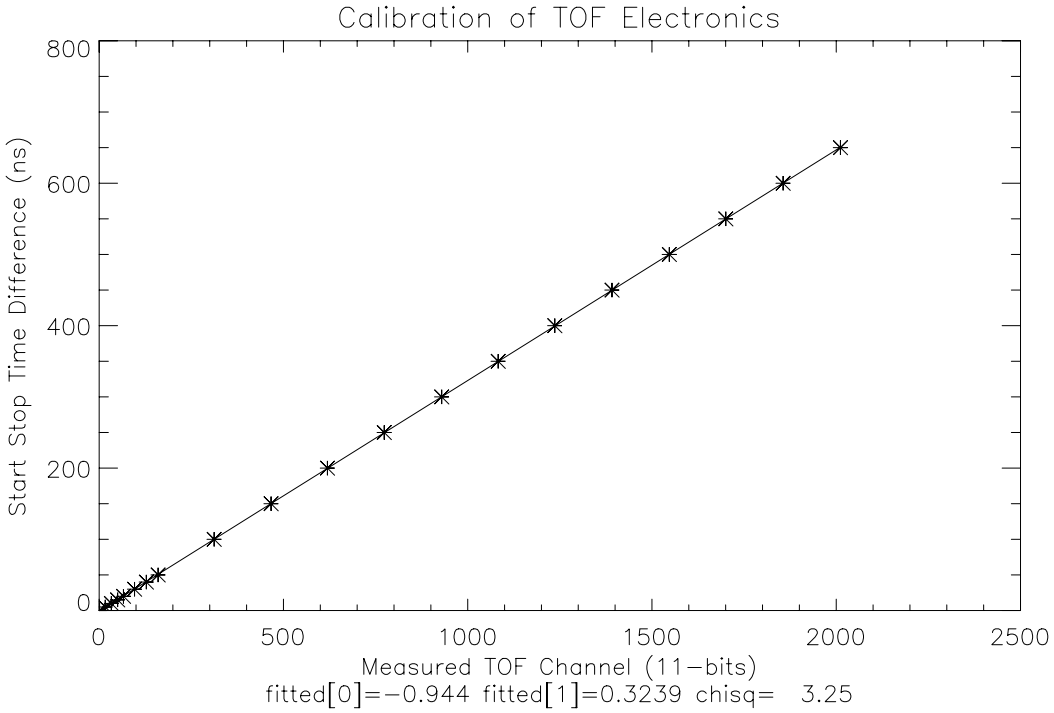

Figure 9. Linearity calibration of time-of-flight and the TOF channel.

A summary of the results of calibration tests performed on the flight electronics to determine the relation between raw data products and the associated physical units such as TOF, pulse amplitudes of the Wedge, Strip, and Zigzag signals, and housekeeping voltage monitors for the high voltage power supplies is shown in Table 4.

Table 4. Conversion of measured raw values to physical units: Linear equation, y = m x + b, where m is slope and b is offset.

Identification	Read Value	Slope	Offset	Physical Unit
TOF	11-bits	0.3239	-0.944	nano second
Wedge signal amplitude	14-bits	5.92E-4		pico coulomb
Strip signal amplitude	14-bits	5.85E-4		pico coulomb
Zigzag signal amplitude	14-bits	8.06E-4		pico coulomb
Deflection System voltage	14-bits	0.936882	13.69	Volt
Post-Acceleration voltage	14-bits	-0.91548	-7.5	Volt
MCP voltage	14-bits	-0.1995	- 324.9	Volt

Results of calibration tests performed on the flight electronics to determine the relation between command set point levels for the high voltage supplies, and the associated high voltage output are summarized in Table 5.

Table 5. Conversion of set point level command to physical units: Linear equation, y = m x + b, where m is slope and b is offset.

Identification	Set Point Level	Slope	Offset	Physical Unit
Deflection System voltage	16-bits	0.234557	5.03	Volt
Post-Acceleration voltage	8-bits	-61.05	0	Volt
MCP voltage	8-bits	-13.31	-323	Volt

2. Electrostatic Analyzer (ESA)

The purpose of this test is to analyze the system performance and to compare it with system requirements and also the 3D ion simulations.

Test facility and setup: An ion beam test of the ESA was performed in the subsystem chamber. The beam from the source was not mass filtered, and a Faraday cup monitored current from the source. A laboratory high voltage power supply provided the deflection voltage for the ESA. Figure 10 shows the setup used for mounting the ESA and allowing it to pivot. The aperture of the ESA is located in the middle of the chamber, aligned with the axis of a rotary mechanical feed-through in the top of the vacuum chamber. The elevation angle of the ESA was set manually with the aid of an externally mounted dial. Azimuth was fixed at zero degrees. Alignment accuracy was on the order of 1 degree. A Quantar MCP detector was mounted directly to the back of the ESA. The standard Quantar electronics package was used to determine counting rates and to image the beam exiting the ESA.

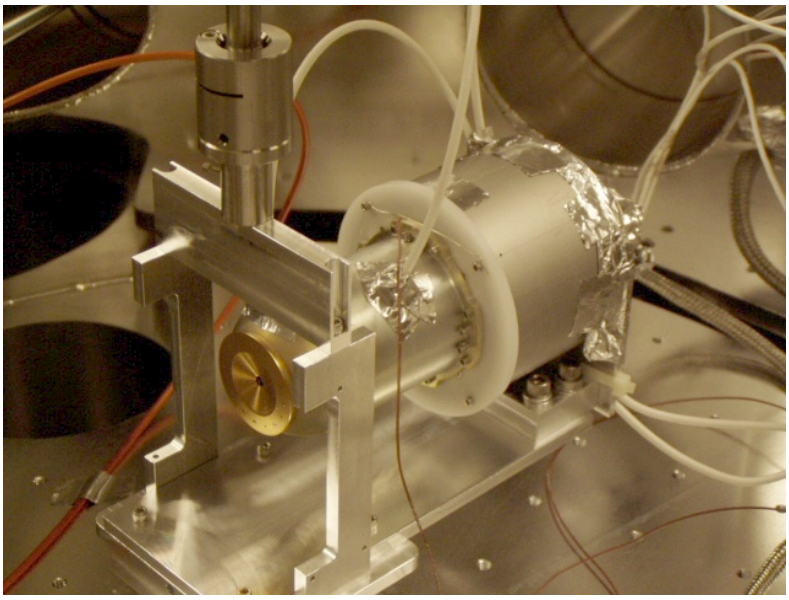

Figure 10. ESA Beam Test Setup.

The purpose of this test was to characterize the ESA, and compare the results with SimIon 3D simulations. It also served as a functional test of the entrance system, before it was integrated with the rest of the sensor. During this test the beam energy was fixed at 2 keV. Measurements were made every 5°, over the elevation angle range (15°< θ < 75°). The ESA was oriented at the desired elevation angle.

The Faraday cup was moved into the beam to determine the ion flux, and then removed. The deflection voltage was stepped in 10 volt increments (< 1 %), and count rates were recorded at each voltage step in order to determine the ESA's transmission as a function of voltage. After this, the deflection voltage was set to its maximum transmission value, and an image was accumulated. The Faraday cup was moved into the beam to check the ion flux rate before the measurements were repeated at the next ESA angle. Once the full range of elevation angles had been mapped, the angular alignment was checked by rotating in the opposite direction. Due to the constraints of the setup the negative angle range was very limited; however, it was possible to span the central 15° blind zone. The measurement made at -16° was similar to the one at +15°, confirming the nominal size of the blind zone, as well as the alignment.

ESA results: Simulations performed with SimIon 3D have been a crucial part of the development of the FIPS ESA. The goal of these simulations was to provide an estimate of the four important performance parameters of this instrument: energy resolution, analyzer constant, angular response and transmission. The simulation geometry is constructed using a programming structure unique to the ray-tracing program. The geometry is laid out in a three dimensional grid, and each grid point is assigned a voltage. The program then solves Laplace's equation for the potentials and fields between the simulated electrodes. Simulated ions were then introduced to the system, and their trajectories tracked and recorded for later analysis.

The grid size used in the simulated geometry must be of sufficient resolution to model all the important features of the entrance system. An outline of how this was done follows: The SimIon program allows the use of mirror symmetry, different grid sizes for separate regions within the ion bench model, as well as repeated instances of selected parts of the model in order to save memory resources. These techniques were used wherever possible in order to make efficient use of the computing resources available. The grid size selection was based on the resolution needed to represent accurately the parts, and to ensure that ion trajectories are far enough from, and will be unaffected by, any field irregularities introduced by the grid structure of the electrode surfaces. The coarsest resolution used to model the ESA was 10 grid points per millimeter. Collimator plates were rendered at 50 grid points per millimeter, the finest resolution used.

To evaluate the performance of the design, a Monte Carlo simulation was performed. The standard simulation injected a cold ion beam at a set of elevation angles covering the angular range of the instrument ($15° < \theta < 75°$). Each transmitted ion's initial and final energy, direction and position were stored for analysis. This information was used to generate estimates of the instrument's performance characteristics, including the analyzer constant, energy resolution, and total ion transmission summed over energy. This data as well as the ion exit position were plotted as a function of entrance angle. In order to compare the ion beam measurements with the Monte Carlo simulations, similar results from both are plotted on one graph. Figures 8, 9, 10, and 11 show respectively the results for analyzer constant, energy resolution, ion exit location, and normalized transmission as a function of elevation angle.

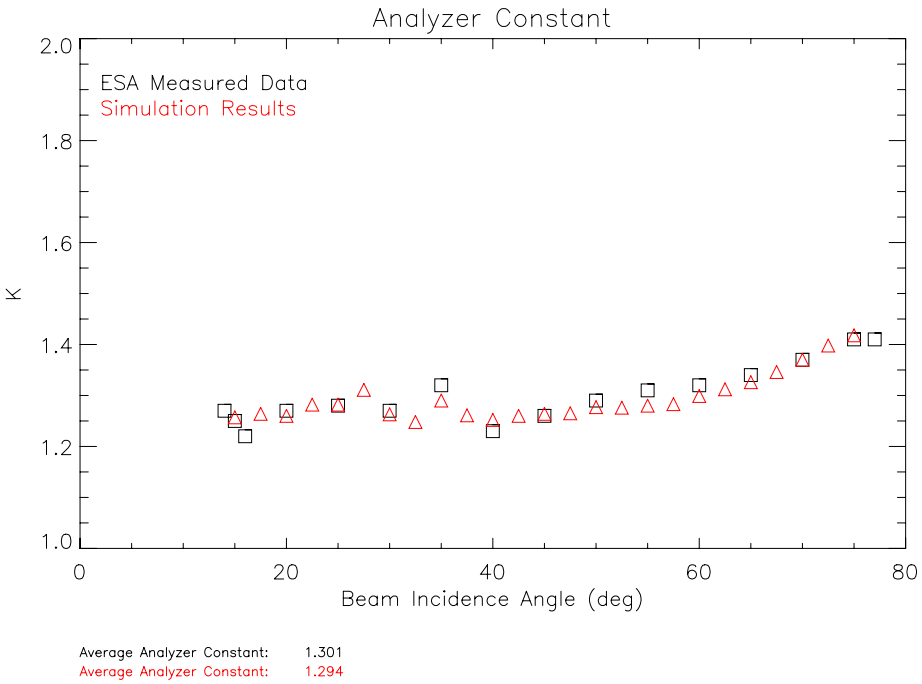

Figure 11. Simulated and measured analyzer constant as a function of elevation angle (relative to the symmetry axis of the FIPS sensor).

Figure 11 shows comparisons of measurements and simulations of the analyzer constant, $\kappa = \frac{E/Q}{U}$, the ratio of the E/Q of transmitted ions, and the deflector voltage. κ is relatively constant, and lies in the range of 1.25 up to 1.4. For a maximum deflector voltage of U=15 kV, this will allow a maximum energy pass-band around 20 keV/e as required.

Figure 12 shows energy resolution measurements as a function of incidence angle relative to the detector's symmetry axis. First of all, the figure indicates an angular range from ~15 to ~75 degrees, as required. There is excellent overall correspondence between simulations and experiments, even though the experimental results seem to indicate a slight, ~1% increase over the simulated result. This small deviation is due to two principal reasons. First, the simulated beam is completely collimated, whereas the experimental beam used here has a ~1 degree divergence, increasing the energy acceptance, as observed. Second, the ESA collimator system has to be manufactured to specifications that were less stringent than the simulated, ideal geometry. The collimator is an assembly of many thin chemically etched plates. The smallest features that can be created are of the order of the thickness of the material, which is 0.05 mm. The smallest features in the collimator are ring segments 0.075 mm wide. The dimensional accuracy of the fabrication process limits the ability to locate features to roughly ±0.013 mm. There are also errors in position or alignment of the individual plates in the collimator assembly, which we estimate to be roughly ±0.013 mm. Since the collimator defines the allowed ion trajectories by acting as a beam stop, the affect of the alignment errors in the assembly is to make the small open channels smaller. An attempt was made to compensate for this effect by making the open channels slightly smaller in the simulation than in the fabricated parts. We attribute the discrepancies between the simulation results and the measured results to manufacturing limitations and assumptions about the size

of the openings in the model. Despite the fabrication issues, the overall acceptance is surprisingly homogeneous, and, on the average, is consistent with the specification of 5% energy resolution.

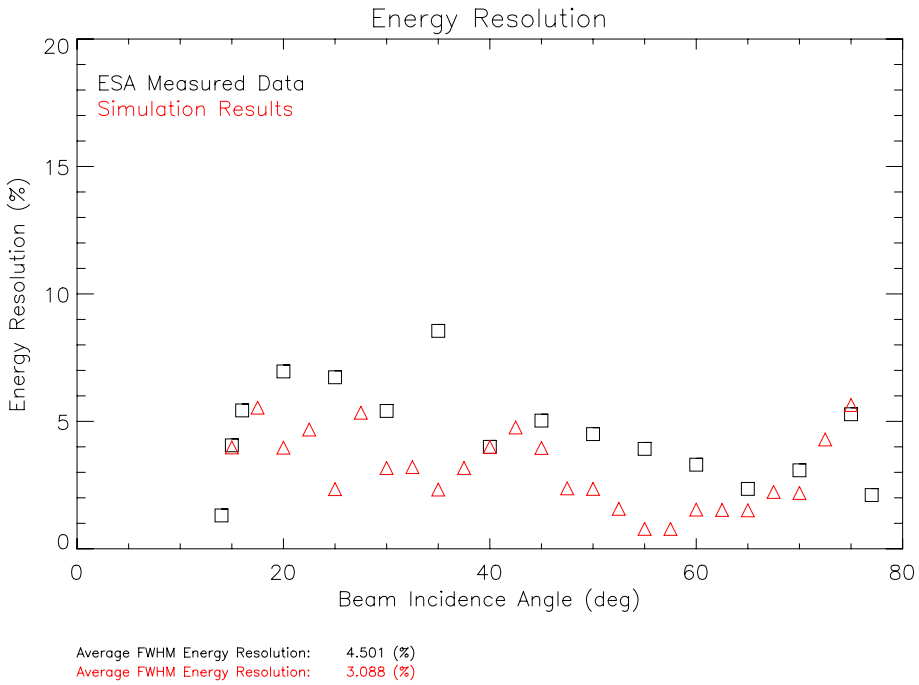

Figure 12. Energy resolution measurements compared with Monte Carlo simulations.

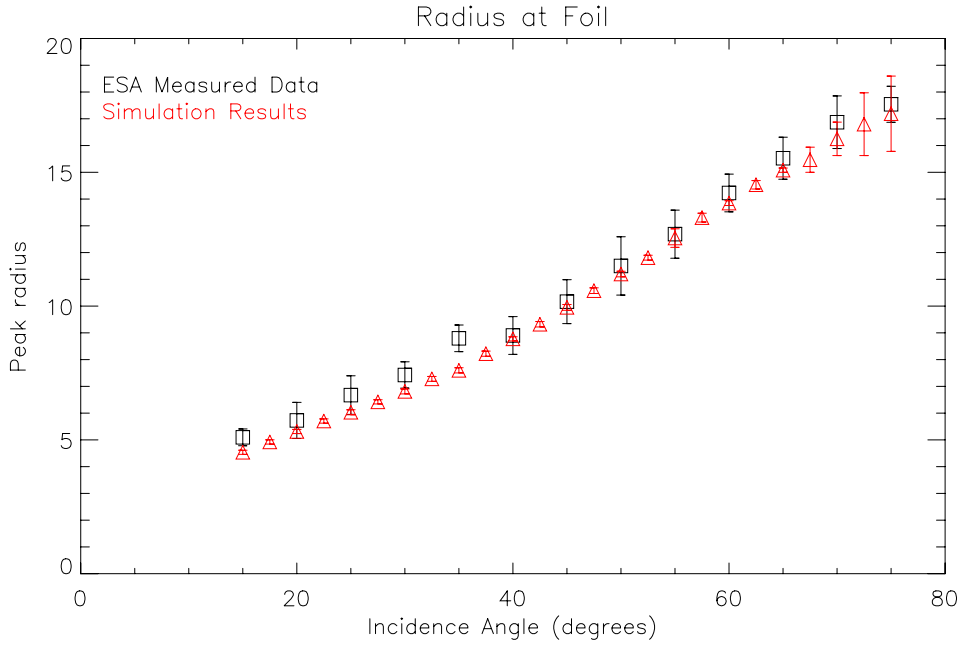

Figure 13. Position of peak radius as a function of incident angle.

FSCM NO.	SIZE	DRAWING NO.	REV.
88898	A	7384-9472	A
SCALE	DO NOT SCALE PRINT	SHEET 21 of 42	

Figure 13 shows the position of the transmitted peak as a function of incidence angle. The radial position is in very good agreement with the simulated results. This relates to the angular resolution requirement of 20 deg, which results in a spatial resolution requirement of 1.5 mm. This is easily achieved, except at the very end of the field of view, where the overall transmission is very low. Within the range of ~15-75 deg, the specification is fulfilled.

Figure 14 shows the normalized total transmission of the ESA. First, this parameter is generally in very good agreement with the simulations. Generally, it is slightly smaller, for the same reasons explained when discussing the change in energy resolution previously. The transmission is generally within 25% throughout the entire angular-acceptance range. One data-point deserves further discussion. It is measured at elevation angle of 40 deg. The transmission at this specific angle is affected fringe-fields at the edge of the so-called field-free regions. This effect is not modeled accurately in the current ion-optics simulation, but will be included in the instrument forward model. The size of the effective aperture, together with energy acceptance and angular range determines the sensitivity, as discussed below.

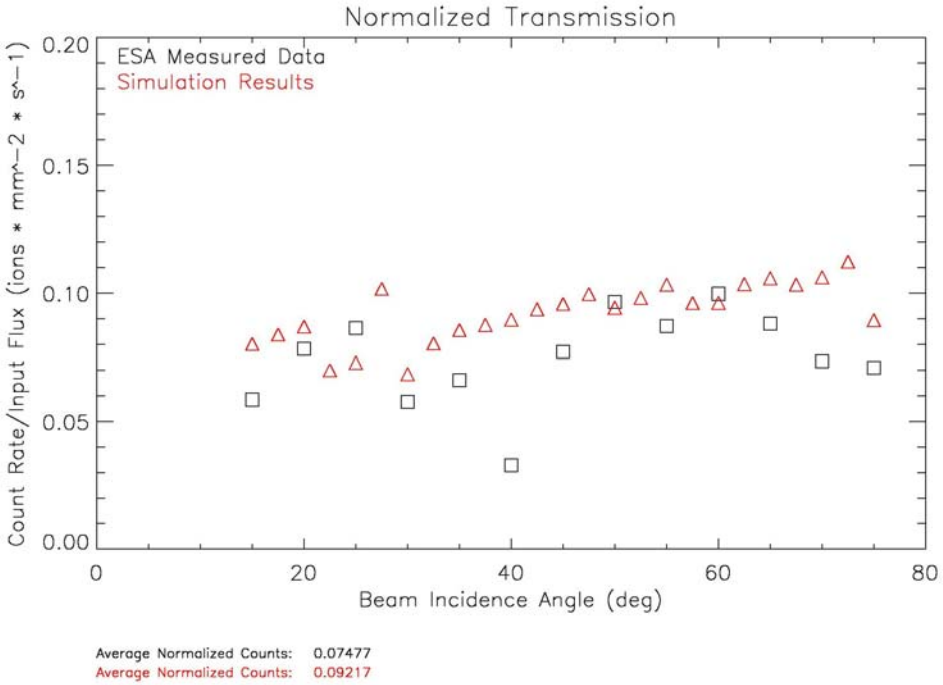

Figure 14. Transmission of FIPS as a function of elevation angle.

The geometric factor is the overall sensitivity of the system. It is one of the key parameters which must be sized very carefully. Based on Mercury magnetospheric and inner heliosphere solar wind simulations, the geometric factor should be 0.1 mm^2 sr eV/eV, The geometric factor is sized such to make sure that there are <100,000 ions per second under normal solar wind and magnetospheric conditions.

The geometric factor is calculated by integrating the measured effective aperture over the tested ranges of particle energy, and then over the solid angle of the field of view. The measured value of the geometric factor is 0.1 mm^2 sr eV/eV, which meets our specifications.

3. Efficiency

The efficiency, ε, of the FIPS instrument is determined by the carbon foil secondary electron response, energy straggling, and MCP response. The purpose of the efficiency measurements is to determine tie-points of a more general instrument model that will be applied to de-convolve FIPS data. This model includes start and stop efficiencies, as a function of angle of incidence (which maps directly to a particular location on the MCP), that are independently measured as part of this process. Note the dependence of the efficiency on two major variables, M, the ion mass, and E_{tot}, the total energy of the ion which is equal to $Q(E/Q + V_a)$. The total energy is varied by changes of E/Q and V_a.

Test setup: For this series of tests, the flight-version FIPS TOF telescope and electronics were mounted in the Calibration chamber behind a pinhole mask, as seen in Figure 15. Using two linear translation stages, the telescope could be moved to position the pinhole at any XY position.

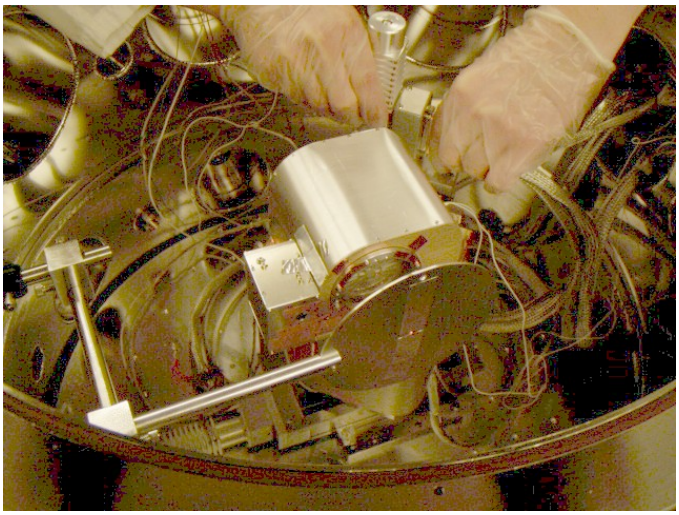

Figure 15. Test setup for total efficiency measurements.

Before measuring the TOF telescope efficiency, it was necessary to determine the optimum bias for the Start and Stop MCP stacks. Cold H^+ and N^+ beams of 5, 10 and 15 keV energies were sent into the system, and the START and STOP efficiencies were measured for bias settings ranging from 2200 V to 2700 V. An MCP bias of 2600 V was determined to be the best setting, consistent for both species, over all energies. This voltage was used for all the remaining calibration tests (it is also planned to be the flight MCP bias level). Sample START and STOP efficiencies for 10 keV N and H beams are shown in Figures 16 and 17, respectively.

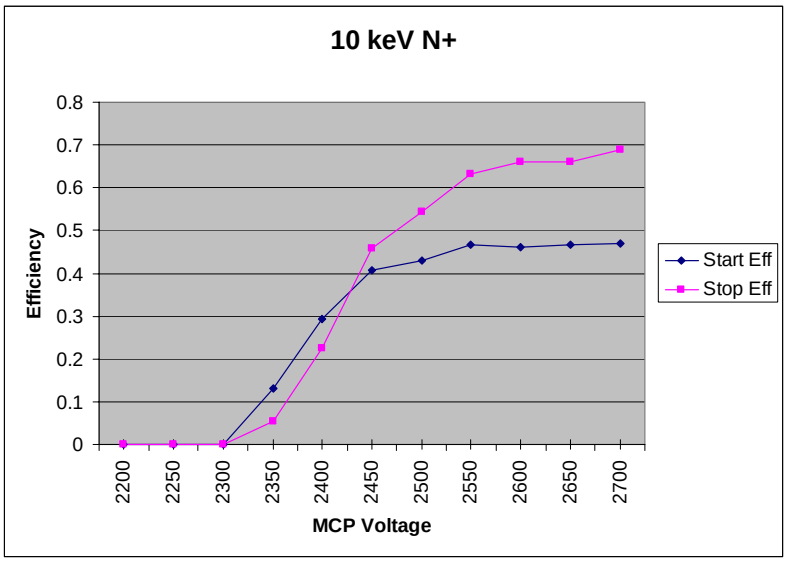

Figure 16. N^+ start and stop efficiencies.

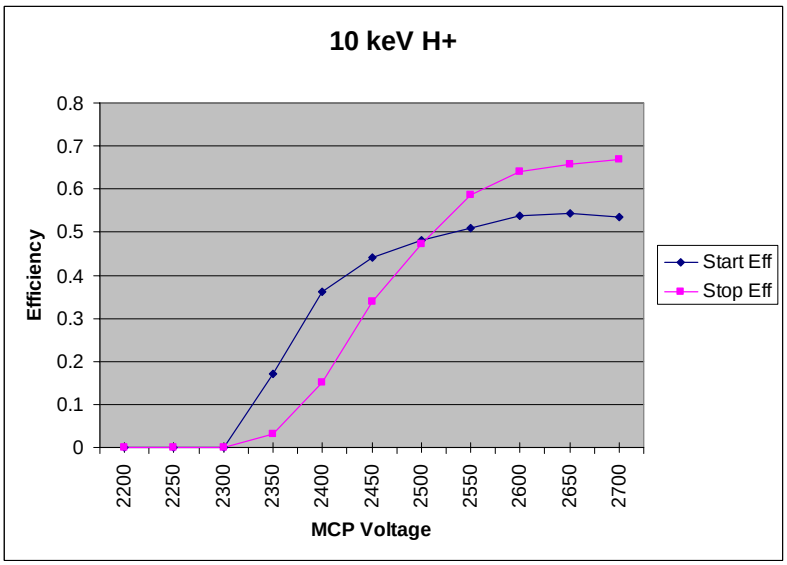

Figure 17. H^+ start and stop efficiencies. The efficiency curves define an MCP voltage in the range of 2.65 kV. At this setting, the efficiency is well behaved and levels off to an approximately constant point.

Position Sensitive Efficiency: Using a cold plasma beam, the TOF telescope was mapped over a grid with 5 mm spacing, and the appropriate efficiencies were calculated. During the later full calibration runs, efficiencies for cold beams of particular masses and energies were recorded at one of these XY locations to act as tie-points, so that efficiencies could be extrapolated for all masses, energies and positions on the carbon foil. Mixed plasma efficiencies can be seen as a function of carbon foil position in Figures 18, 19, and 20, and species/energy efficiencies are seen in Table 6. MCP-average values for the START, STOP and Double efficiency are 0.38, 0.60 and 0.19, respectively.

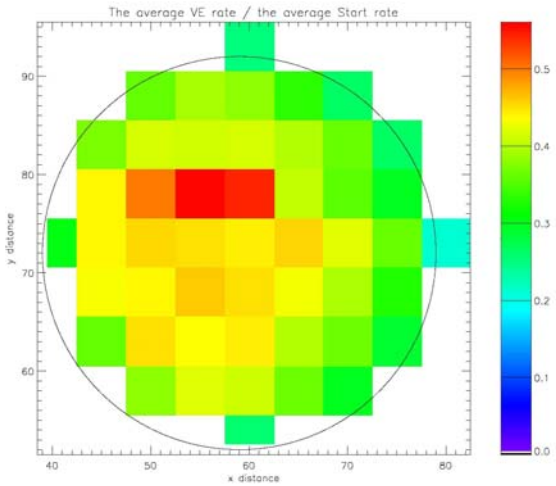

Figure 18. Start efficiency for the FIPS TOF telescope.

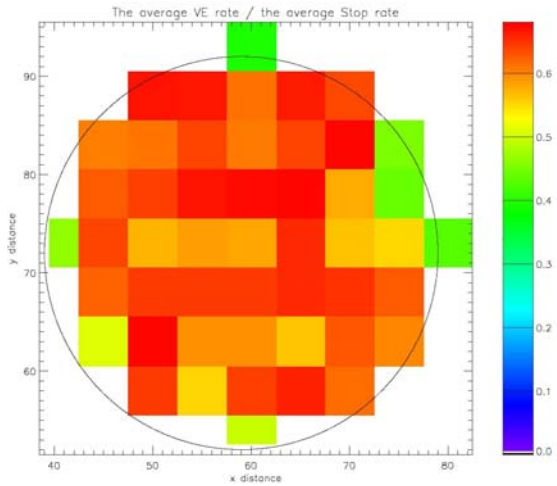

Figure 19 - Stop efficiency for the FIPS TOF telescope.

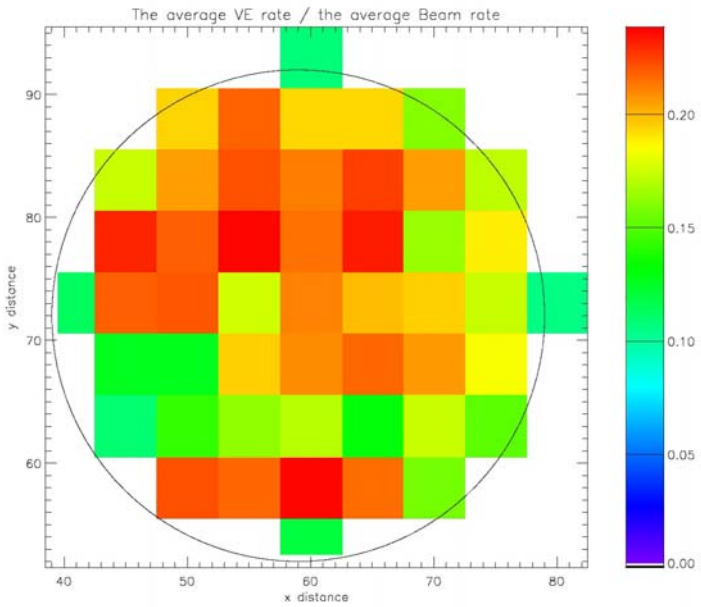

Figure 20 - Double efficiency for the FIPS TOF telescope.

The overall efficiency is slightly position dependent. That should be expected to be caused by the position dependence of the START efficiency.

During the full calibration phase of FIPS, START and STOP efficiency data were recorded for the θ=35, φ=51 position of the FIPS system. This corresponds exactly to one of the grid points measured on the previous TOF telescope efficiency tests. From this tie point, TOF efficiencies can be calculated for the species and energies found in Table 6. These test runs cover the entire mass and energy ranges of the FIPS instrument.

Table 6. Species and energy START and STOP efficiencies. VE in these tables stands for "Valid Events".

VE/START RATE						
Energy	H	N	H2O	N2	O2	Ar
10	0.5167137	0.3800458	0.3250036	0.2858347	0.2758546	0.2150582
15	0.5386723	0.4548879	0.3954761	0.3661765	0.357049	0.2874639
17	0.5409178	0.4827809	0.4248952	0.3955157	0.3788202	0.3122514
20	0.5160804	0.4864326	0.4655375	0.426834	0.4195319	0.342901
25	0.5431305	0.4756488	0.5169731	0.4809008		0.3579027

VE/STOP RATE						
Energy	H	N	H2O	N2	O2	Ar
10	0.5865179	0.6167282	0.5474601	0.5150901	0.5069346	0.453567
15	0.6625322	0.6506596	0.5690449	0.5512067	0.5281351	0.5015872
17	0.6244907	0.6817063	0.5829358	0.5956665	0.5781816	0.4896816
20	0.8730316	0.6789182	0.6123913	0.557133	0.5729703	0.5325825
25	0.6779457	0.525527	0.6295137	0.6464469		0.5781826

4.0 Mass Resolution

The mass resolution of a TOF instrument is directly tied to the measured time-of-flight of the incident particle. We know the time of travel τ between the carbon foil and the anode, and the distance d traveled in that time. The ESA voltage step and analyzer constant gives us the particle's E/Q from

$$\frac{E}{Q} = Vk \,.$$

This energy per charge is modified by the post-acceleration voltage U and the energy loss from the foil ε, so the velocity $(d/\tau)^2$ and E/Q information from the ion's impact location gives us the mass per charge [Gloeckler, 1979, 1990],

$$\frac{M}{Q} = \frac{2(Vk+U)\varepsilon\tau^2}{d^2} \,.$$

The mass per charge resolution is then

$$\left(\frac{\Delta\frac{m}{Q}}{\frac{m}{Q}}\right)^2 = \left(\frac{\Delta\alpha}{\alpha}\right)^2 + \left(2\frac{\Delta\tau}{\tau}\right)^2 + \left(2\frac{\Delta d}{d}\right)^2 + \left(\frac{\Delta kV}{kV}\right)^2 \left(\frac{1}{1+\frac{U}{kV}}\right)^2 ,$$

where $\Delta\alpha/\alpha$ is the energy straggling of the ion from its passage through the carbon foil, $\Delta\tau/\tau$ is the uncertainty in the ion's time of flight, $\Delta d/d$ is the uncertainty in the path length of the ion's trajectory through the TOF telescope, and $\Delta(E/Q)/(E/Q)$ is the energy resolution of the electrostatic analyzer.

As an experimental measure of the mass resolution, we fold the energy straggling, path length and timing uncertainty into a single number, measured by taking the width of the TOF spectrum for each

species-energy test run from the Efficiency Calibration series (see section 3). The calculated M/Q is then

$$\frac{M}{Q} = \frac{2(Vk + U)\tau'^2}{D^2},$$

where D is now the physical distance between the carbon foil and the STOP MCP, and τ' is the measured time-of-flight of an incident particle. The new formula for the mass resolution is

$$\left(\frac{\Delta\frac{m}{Q}}{\frac{m}{Q}}\right)^2 = \left(2\frac{\Delta\tau'}{\tau'}\right)^2 + \left(\frac{\Delta kV}{kV}\right)^2\left(\frac{1}{1+\frac{U}{kV}}\right)^2,$$

The mass resolution is then just the TOF and energy resolutions added in quadrature. Table 7 shows the resulting mass resolution trends.

It is important to note here that energies listed in Table 7 are the particle energies after post-acceleration. Given that the maximum energy per charge that will be seen by the carbon foil is 35 keV, we can expect that the mass resolution for magnetospheric and solar wind heavy ions will improve. Additionally, the 10 keV energy values will not be seen at all, given a flight post-acceleration value of 15 keV.

FIPS mass resolution must be such that C, N and O can be separated. The HWHM mass resolution for N in the above table is sufficient for the peak separation.

5. Rate vs. Rate Calibrations

Overview

The purpose of this test is to determine the relation of measured rates in FIPS and the true ion rates. The principal requirement for the entire system is that FIPS can measure a total event-rate of 50,000 Hz. There are three fundamental bottle-necks that could contribute to false rates. First, the FIPS analog circuitry could be too slow to detect ions. Second, the integrated FIPS electronics could be limiting the count rate. Third, the APL built EPU could limit the total throughput.

Due to constraints described in the introduction above, the full end-to-end test of the FIPS instrument including the EPU was not possible. To mitigate such throughput problems, FIPS has a level of functionality that was introduced to allow for suppression of H^+, which should be the most abundant species during the entire mission duration. The purpose of this suppression mechanism is to save computational resources by only analyzing a fraction of the H^+ incidence directions.

The calibrations include two parts: First, a total versus apparent rate measurement is performed to determine the total throughput of the FIPS electronics. Second, the H^+ suppression function was calibrated and its linearity assessed.

Table 7

Species	Beam KE (keV)	Dt/t	DE/E	D(M/Q/(M/Q) (FWHM)	D(M/Q/(M/Q) (HWHM)
H	10	2.60%	5.00%	7.21%	3.61%
	15	6.70%	5.00%	14.30%	7.15%
	17	3.60%	5.00%	8.77%	4.38%
	20	3.90%	5.00%	9.26%	4.63%
	25	4.60%	5.00%	10.47%	5.24%
N	10	9.80%	5.00%	20.23%	10.11%
	15	6.20%	5.00%	13.37%	6.69%
	17	4.90%	5.00%	11.00%	5.50%
	20	3.60%	5.00%	8.77%	4.38%
	25	2.00%	5.00%	6.40%	3.20%
H20	10	12.80%	5.00%	26.08%	13.04%
	15	9.30%	5.00%	19.26%	9.63%
	17	8.60%	5.00%	17.91%	8.96%
	20	7.90%	5.00%	16.57%	8.29%
	25	10.90%	5.00%	22.37%	11.18%
N2	10	18.40%	5.00%	37.14%	18.57%
	15	13.40%	5.00%	27.26%	13.63%
	17	12.00%	5.00%	24.52%	12.26%
	20	9.80%	5.00%	20.23%	10.11%
	25	7.00%	5.00%	14.87%	7.43%
O2	10	28.20%	5.00%	56.62%	28.31%
	15	16.80%	5.00%	33.97%	16.98%
	17	13.60%	5.00%	27.66%	13.83%
	20	13.10%	5.00%	26.67%	13.34%
	25	N/A	N/A	N/A	N/A
Ar	10	55.30%	5.00%	110.71%	55.36%
	15	23.50%	5.00%	47.27%	23.63%
	17	19.50%	5.00%	39.32%	19.66%
	20	19.20%	5.00%	38.72%	19.36%
	25	13.80%	5.00%	28.05%	14.02%

True vs. Apparent Rates

Purpose: The purpose of this test is to determine the total throughput of the FIPS electronics.

Method:

1. Reliably determine the incident ion flux.
2. Register Start, Stop, and valid Coincidence pulses, and calculate start and stop efficiencies.
3. Determine true vs. apparent rate for a cold plasma beam.
4. Determine proton true vs. apparent rate as a function of suppression threshold.

For this test, the FIPS system was oriented to the θ=35, φ=51 position, as done for the species efficiency tests. A beam profile was measured such that we could reliably predict the beam peak measurement based on the measurement of the beam 3.5 cm away – this allowed us to use a much higher intensity beam than the channeltron could measure without saturating. For each of four mixed plasma beams seen in Table 8, the START, STOP and Double coincidence (or Valid Events VE) rates were recorded.

In a "perfect" instrument, a set increase in beam intensity would produce an identical increase in the recorded rates, i.e., a factor of two increase in the beam intensity would produce a factor of two increase in the recorded rates. However, due to the finite speed of modern electronics, most instruments record a degradation of counting rate efficiencies as the input flux increases.

Results: Table 8 lists the percentage of expected counts actually recorded by FIPS as a function of beam intensity. Only at the highest beam flux does any rate drop below 50% of the ideal value, corresponding to a VE rate of 12 kHz. This calibration curve therefore allows for an after-the-fact correction for measured rate in the entire measurement interval specified above.

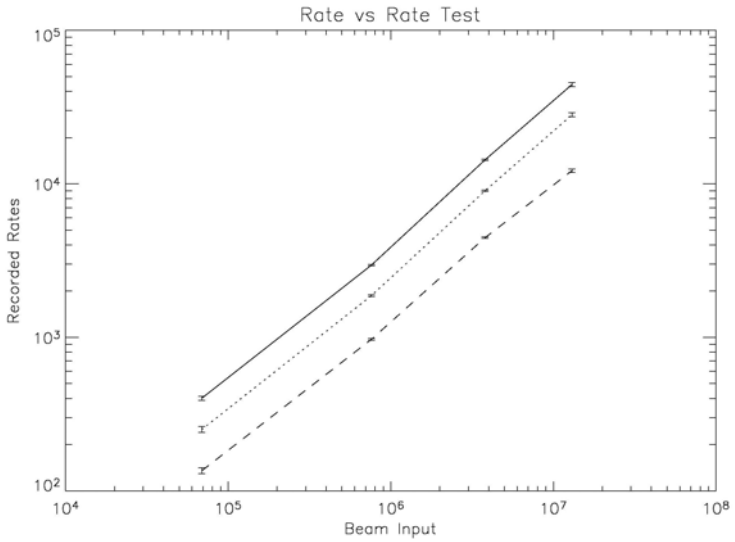

Figure 21. Rate vs Rate test results for START (dotted line), STOP (solid line) and Valid Events (dashed line) rates.

Table 7. Results from True vs. Apparent Rate.

Filament Setting	Beam (c/s)	START	STOP	VE
60%	6.88E+04	100.00%	100.00%	100.00%
65%	7.60E+05	66.69%	67.39%	65.00%
70%	3.80E+06	64.72%	65.05%	59.73%
75%	1.30E+07	58.50%	59.34%	47.64%

True Versus Apparent Rate, including Proton Decimation Test

Purpose: The purpose of this test is to determine the total throughput of the FIPS electronics and the function of the ion suppression function.

Method: As indicated above, the FIPS instrument has the capability of suppressing proton measurements. As the solar wind is > 95% protons, this capability effectively increases the dynamic range of the system, allowing it to measure rare ion populations without being swamped by the dominant species.

The suppression threshold of FIPS is completely user-defined. That is, an arbitrary TOF channel is selected as the threshold, and any events recorded in a lower channel are suppressed by a user-set factor of 1, 2, 4, 8, 16, 32, 64, or 128. To test the suppression function of the FIPS instrument, the suppression threshold was set to the middle of the N_2 peak, 263 ns. A 5 keV cold mixed plasma beam was sent into the system, and a baseline TOF spectrum was recorded. The rejection level was set to factors of 2, 4, 8 and 64, and new TOF spectra were recorded for each setting.

Results: Figure 22 shows the recorded suppression ratio as a function of rejection factor. This was plotted from data shown in Table 9. We clearly see that the suppression technique works very consistently. The average ratio of measured suppression to commanded suppression (including only ratios greater than one) is 0.953, with sigma = 0.012. . This calibrated result will allow for a careful retrieval and correction of suppressed H+ counts.

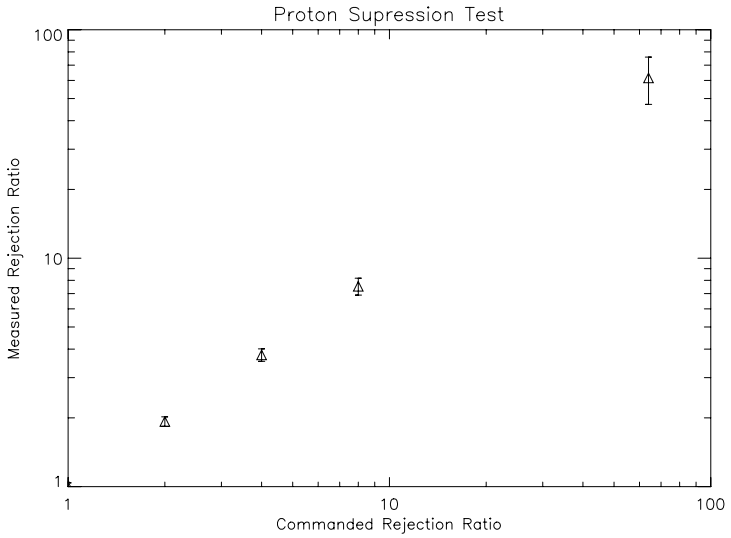

Figure 22. Suppression threshold test. The measured rejection ratio agrees almost perfectly with the commanded rejection ratio.

Table 8. Results from the Proton Suppression Test.

Commanded Suppression Ratio	Measured Suppression Ratio	Measurement FWHM	Ratio of Measured Suppression to Commanded Suppression
None	1.00	0.0391	1.00
2	1.928	0.0932	0.964
4	3.773	0.237	0.943
8	7.535	0.642	0.942
64	61.541	14.39	0.962

6. In-flight Analysis Tools

Position measurement calibration: The measured position indicates an ion's incidence angle, or the direction of the velocity vector. Ideally the E/q of ions that pass through the ESA would depend only on the deflection voltage, and be independent of the ion's entrance angle. We have measured the ESA's analyzer function (the ratio of energy per charge of passing ions to the applied ESA electrode voltage as a function of incident ion angle). These measurements show that the analyzer function is nearly independent of angle, and it is treated as such for the on-board data analysis. However, the position information, in tandem with the system's analyzer function, allows an improved measurement of an ion's energy per charge for ground-based analysis. This information produces a three-dimensional distribution function for the ambient plasma, from which other important parameters can be calculated.

The start micro-channel plate utilizes a wedge/strip/zigzag anode for position measurement by the charge division technique [Anger, 1966]. Measuring the charge deposited on each of the three anodes enables the calculation of a two-dimensional position for each event. If the event is not a proton to be decimated, the signal amplitudes are digitized and sent to the EPU, where the x-y position of the event is determined. Due to stray capacitance between the wedge, strip, and zigzag anodes, there is signal coupling, or crosstalk, that creates position distortion. A Spice simulation which included the front end electronics to quantify this effect was performed using measured capacitances of the WSZ anode (it also accounted for gain differences in the three amplifier chains). From the simulation results a simple formula that corrects for most of the crosstalk was developed. This formula is used in the routines that calculate position for the analysis of calibration data. (The on-board event processing software implements an approximation to this formula for the 6-bit x-y position calculation for PHA data, and the 3-bit x-y position calculation for velocity distribution data.)

In order to test the position mapping accuracy of the sensor, the TOF telescope and electronics were mounted in the Calibration chamber behind a stationary pinhole mask, through which a small diameter beam could pass. Using two linear translation stages, the telescope could be moved to locate the pinhole at any desired x-y position. This setup was also used for the efficiency measurements. A cold mixed plasma beam was used to map the TOF telescope position response over an x-y grid with 5 mm spacing. The measured positions, along with points showing the x-y location of the beam are plotted in Figure 20.

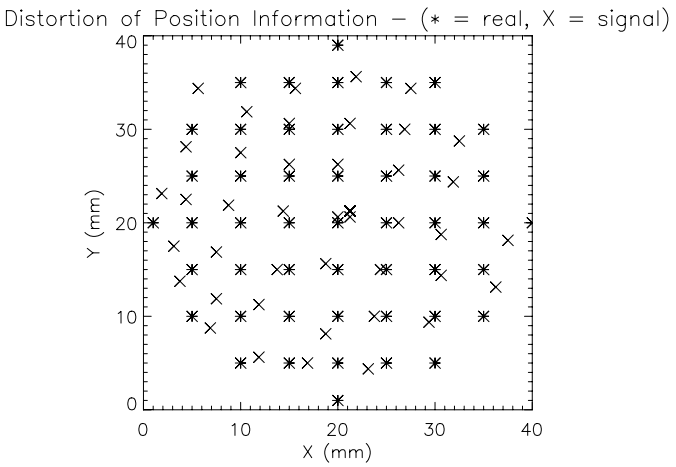

Figure 23. Test of in-flight calibration of the position sensing function. The differences between measurements (*) and real position (x) are used do calibrate the ground-based analysis routine for position sensing.

7. UV Background Suppression

UV suppression requirement: The purpose of this test is to demonstrate that the ESA sufficiently suppresses ultraviolet light that enters through its aperture. The worst case is an equivalent of 11 suns. First the intensity of the UV bulb for a given input power was determined, and then the UV transmission of the ESA was measured as a function of source angle.

Ultraviolet photons can produce background counts in the Carbon foil, or, cause background on the Stop MCP. The large majority of all EUV photons are 121.6 nm, H Ly-α. The total flux of these photons over the solar cycle changes to within a factor of two, but typically is around $\Phi_\gamma = 5 \cdot 10^{11}\ phcm^{-2}s^{-1}$ [Jursa, 1985]. The secondary electron yield in a Carbon foil is $\varepsilon = 8 \cdot 10^{-4}\ e/ph$ [Hsieh et al., 1980]. With an aperture of $A = 2 \cdot 10^{-2} cm^{-2}$, the total secondary electron flux is therefore

$$\Phi_e = \Phi_\gamma A \varepsilon \varsigma \,. \qquad (4)$$

Here, ζ is the suppression factor that is calculated here. We specify the secondary electron flux to $\Phi_e < 0.1$ e/s, based on the overall background specification. The EUV suppression factor of the electrostatic analyzer is therefore specified to be 1.25×10^{-8}. Due to the low efficiency of MCPs this also takes fulfills the specification on noise of the Stop MCP.

To be certain that the FIPS instrument meets this suppression requirement, the test is done in two parts. First, the transmission of the ESA to UV is measured using a very bright UV lamp. Second, the overall background count of the integrated instrument is measured.

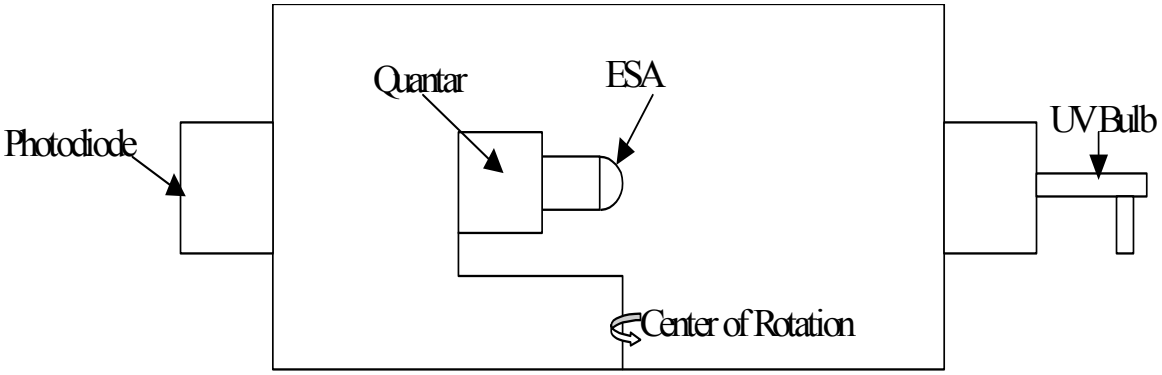

Figure 24. ESA UV test chamber setup.

Our specification requires that there must be less than 1 double-coincidence count per second due to UV photon or secondary electron entry or generation in the system. The FIPS TOF window is 667 ns, which by the relation

$C = r^2\Delta t$ [Knoll et al., 2000]

(C is the maximum DC count rate, r is the noise even rate, and Δt is the TOF timing window) gives us a maximum noise singles rate due to UV photons or secondary electrons scattered out of the foil by UV photons of 1224 counts/s. Therefore, to meet our specifications, the FIPS instrument must record no more than 1224 noise counts per second.

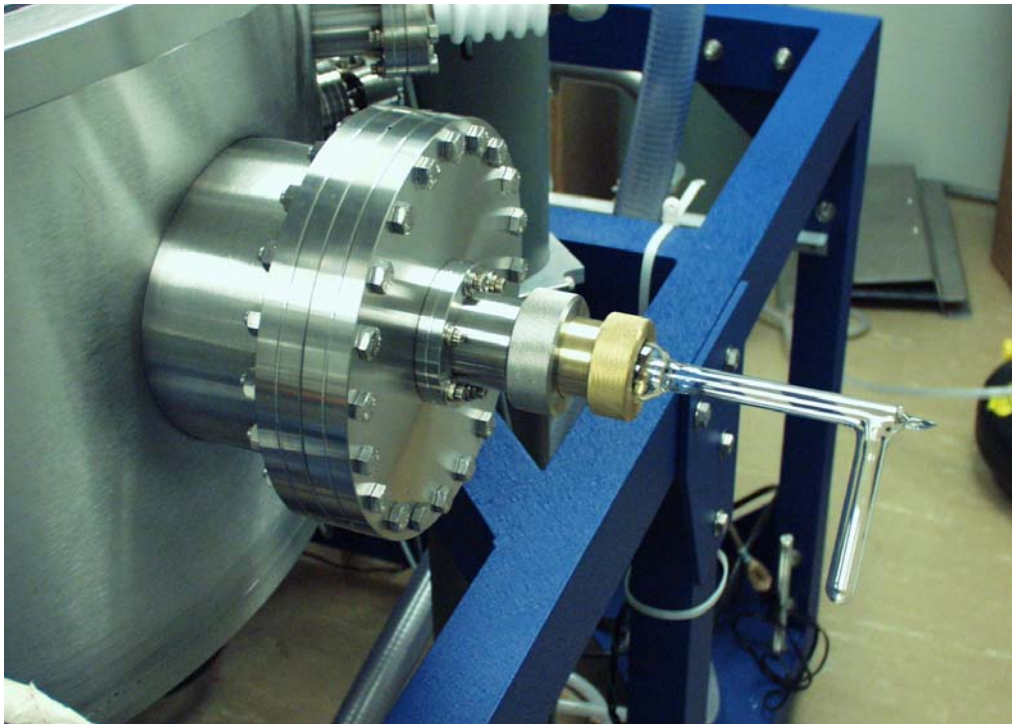

Figure 25. Vacuum Ultraviolet Bulb.

Test setup: The ESA ultraviolet test was done in the subsystem chamber also used for the ESA ion beam test. The set up is shown in Figure 10 and Figure 24. The aperture of the ESA is mounted in the exact middle of the chamber so it can be located at the pivot point. A shaft shown at the top connected to an externally mounted dial that could be moved to rotate the ESA. The accuracy was 1 degree. A Quantar MCP detector was mounted directly to the back of the ESA in a sealed enclosure, so that only photons that go through the ESA are detected. The Quantar covers the full area of the ESA output. The UV bulb (from Opthos Instruments) is a line source emitting primarily in the Lyman-alpha region (121.6 nm). There is 10% H and 90% Ar present in the bulb and it is excited by a microwave source. This bulb is shown connected to the chamber in Figure 25. Figure 24 shows that the photodiode is mounted across from the bulb to measure its intensity. The photodiode is an absolute XUV silicon diode with an area of 1 cm^2.

In order to determine the lamp intensity we used the relation:

$$photons = \frac{I}{q \bullet \varepsilon} \tag{5}$$

where I is the current, q is the elementary charge of 1.6×10^{-19} C and ε is the efficiency of the photodiode (1 at VUV wavelength). It is assumed that 1 Sun is equivalent to 5×10^{11} photons/cm^2. The intensity at the halfway point between the bulb and the photodiode is assumed to be 4 times the intensity at the photodiode since that the intensity varies with the square of the distance from the bulb. Since the area of the photodiode is 1 cm^2, the UV flux at the ESA can be computed. There were two trials of operating the lamp at various wattages, and the results are shown in Figure 26.

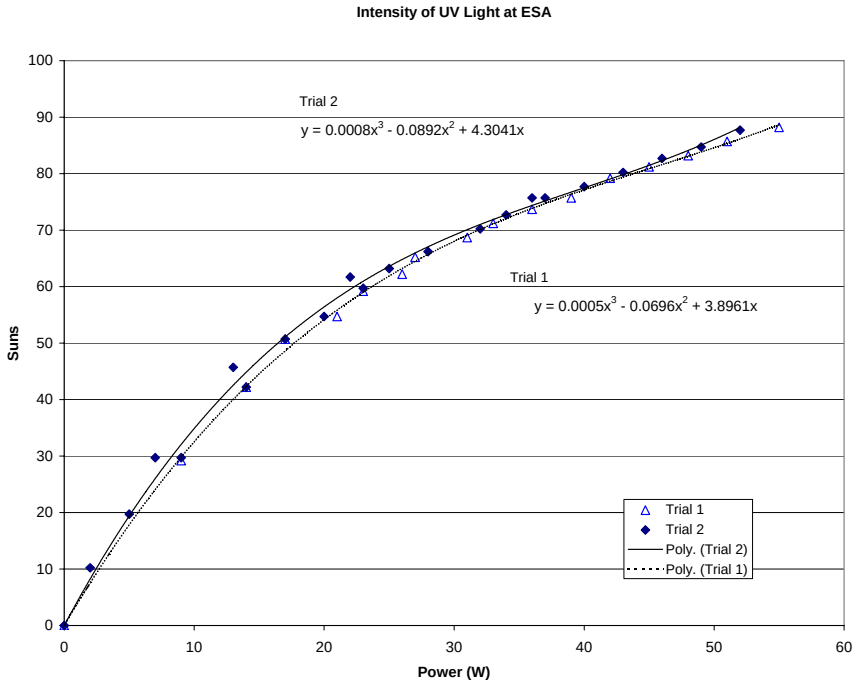

Figure 26. Intensity of UV at the ESA Aperture Based on Lamp Power.

Test results: The ESA was tested over its full angular range with the UV lamp operating at 26 W. This corresponds to approximately 60 Suns in the UV range. The pulses from the Quantar were accumulated for 30 seconds in order to determine an average count rate at each angle. The ESA is considered at 0 degrees when it is facing the lamp. The result is shown in Figure 27. Background counts in Figure 27 are a combination of UV photons striking the Quantar, as well as counts from secondary electrons generated by passing UV photons. The Quantar has a UV detection efficiency of 1%, which is the same as the flight MCP UV efficiency. Secondary electrons are generated with an efficiency of 8×10^{-4} e/ph [Hsieh et al., 1980]. In Figure 27, we see that one Sun of UV radiation produces approximately 1.6 counts/s in the Quantar. At Mercury, The FIPS instrument will be exposed to UV fluxes 11 times this value, resulting in a UV-generated background count of 18 counts/s. This value is a factor of 70 better than our specifications.

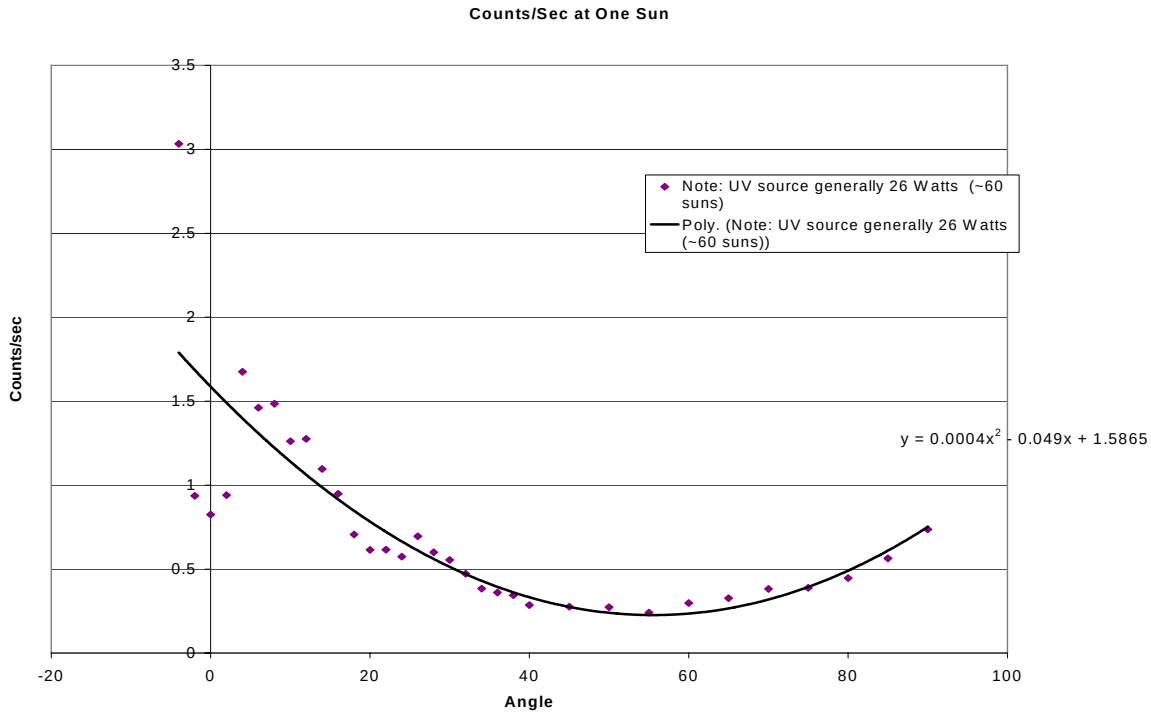

Figure 27. Average Counts Received at One Sun If this plot is scaled to the expected 11Sun input at the orbit of Mercury, FIPS will record a maximum of 18 counts per second.

Integrated Instrument Test: A UV light test was also performed on the complete sensor before delivering it to APL. The same light source was used as for the ESA UV suppression test. However, for this test the UV source was moved to the ion beam calibration chamber using the same instrument configuration as used for the integrated ion calibrations. In this setup, FIPS was located near the center of this chamber on the two-axis rotational mount used for the calibration. Initially, the counting rates were higher than expected from the ESA test. The reason for the light leak was apparent after the vacuum chamber was opened and an examination was performed. There were some very small openings where

light could enter the TOF system producing exactly the measured angular dependences and profiles of the transmitted light. These cracks were successfully sealed.

CALIBRATION SUMMARY

Table 9 - Summary of calibration results

Requirement	Value	Measured
Energy Range	50 eV – 20 keV	Sufficient
Energy Resolution	10%	4.5%
Angular Range [sr]	1.4 π	1.4π
Angular Resolution [FWHM]	20°	15°
Instantaneous Dynamic Range	10^5	10^5
Mass/Charge Range	1-30	1-40
Mass/Charge Resolution [Δ(M/Q)/(M/Q)]	Sufficient to separate C,N,O	Sufficient
Geometric Factor	0.1 mm^2 sr eV/eV	0.1 mm^2 sr eV/eV
Maximum allowable valid count rate	10^5	10^5
Maximum allowable background count rate	1 kHz	18 Hz

FIPS SCIENCE DATA PRODUCTS

The FIPS average bit rate is 81 bits per second, which resulted in a concerted effort to maximize the science content of every byte coming back to the Science Team, while minimizing wherever possible the size of the data packet. This section describes the data products we expect to receive from the spacecraft, and how they are created. The reader is referred to document number JHU/APL 7389-9041 (from which this section is derived) for more details.

Mass and Energy Spectra:

- One 256-element mass distribution histogram (accumulated over each 10-scan sequence)
- Five 64-bin element energy spectra (one for each of the 5 energy vector ranges) (accumulated over each 10-scan sequence)

The EPPS software maintains a number of 68-element tables that are used in performing DSHV scan sequences. Each of the 68 table entries has the following format:

Settling time (8 bits)	Dwell time (8 bits)	DSHV level (16 bits)	TOF threshold (16 bits)

Each table entry specifies the settling time, dwell time, DSHV voltage level and proton threshold to be used at the corresponding step within a scan. The settling and dwell time fields are expressed in 10 ms time units.

One complete scan is made up of 64 voltage steps and 4 ramp-up steps. Ten consecutive scans correspond to one "scan sequence". Table entries for which the dwell time is zero correspond to ramping the DSHV level to its initial value for the scan. Events are disabled for these ramp-up steps. Four out of the 68 table entries correspond to ramp-up steps. The remaining 64 steps correspond to DSHV settings at which events are enabled and processed. (Note that exactly 4 out of the 68 entries must correspond to

zero dwell times and all of the remaining 64 must contain a non-zero dwell time to keep the step index synchronized. The step index is a modulo 64 counter that is only incremented for steps that have non-zero dwell times.)

At each step, the event FIFO is disabled and reset during the settling period for that step. After the settling period expires, event generation is enabled and events are processed for the indicated dwell period. At the conclusion of each dwell period, the EPPS software performs the following actions:

1. Place the FIPS instrument in "stand-by" mode to stop the generation of event data.

2. If this is the conclusion of a 10-scan sequence, signal the FIPS task to:
   - Compress and output the FIPS data in telemetry
   - Clear the FIPS data product buffers

3. If this is not the conclusion of a 10-scan sequence, signal the FIPS task to:
   - set the DSHV to the next voltage level as indicated by the voltage step table
   - set the proton event threshold as indicated by the threshold table
   - Set the settling period to the value indicated in the corresponding table entry.

4. Flush the FIPS event FIFO and place the FIPS instrument into "Manual" mode to start the generation of event data. Set the event collection interval (i.e. dwell time) for the next step.

5. Process events until this dwell time expires.

As events are captured during a particular step within a voltage scan, the following processing is performed for events that are extracted from the FIPS event FIFO:

1. The 9 most significant bits of the TOF value are concatenated with the 6-bit step number (0 through 63) to form a 15-bit index that identifies one of 32K entries in a lookup table. Each element within the table is an 8-bit value that specifies which bin should be incremented within the mass distribution histogram.

2. The index obtained from the lookup table is used to identify which one of the 256 bins to increment within a mass distribution histogram. Each of the 256 mass distribution histogram elements (bins 0 – 255) is maintained as a 32-bit value. Thus the mass distribution histogram is 1K bytes in size (before being compressed for output in the telemetry stream).

3. The bin number obtained from the lookup table is also used to determine whether the associated event falls within one of 5 different energy vector ranges. If so, the current voltage step number is used to identify and increment one of the 64 elements in the corresponding energy vector. Each element in the energy vector is a 32-bit number.(A total of 5*4*64=1280 bytes are required for the five energy vector histograms.)

Proton Velocity Distribution Functions:

- One 8x8 Proton Velocity Distribution Function (accumulated over the first scan in a 10-scan sequence)
- One 8x8 Proton Velocity Distribution Function (accumulated over scans 2 – 10 in each 10-scan sequence)

The EPPS software generates an 8×8 proton velocity distribution function based on the proton events that are detected during the first 64-step voltage scan of each 10-scan sequence. This function corresponds to a matrix whose elements are 32-bit values.
For each proton event processed, an X and a Y value are computed using the same technique as described above.

The values X/8 and Y/8 are used as the row and column within the velocity distribution matrix that corresponds to the element or bin to be incremented.

An 8x8 proton velocity distribution function is also generated for all proton events that are detected during scans 2 through 10 of each 10-scan sequence. This velocity distribution corresponds to a 9-scan accumulation interval.

At the conclusion of a complete scan sequence, the 64 matrix elements for both the single-scan and the 9-scan proton velocity distributions are compressed from 32 bits down to 10 bits each and stored for output in telemetry. Each matrix is then cleared before starting the accumulation of the new velocity distribution functions for the next scan sequence.

Heavy Ion Velocity Distribution Functions:

- Five Heavy Ion Velocity Distributions (one for each of the 5 energy vector ranges) (accumulated over each 10-scan sequence)

The EPPS software generates separate velocity distribution functions for non-proton events that correspond to the 5 energy vector ranges. These five velocity distribution functions are accumulated over each 10-scan sequence. If a non-proton event maps to one of the 5 energy vector ranges, then the same X/8 and Y/8 values are computed for the event (as described above), and the corresponding bin within the selected matrix is incremented.

At the conclusion of the 10-scan sequence, the contents of the 5 non-proton velocity distribution matrices are compressed from 32-bit elements down to 10-bit elements. All 64 elements are compressed and stored for output in telemetry. All five matrices are then cleared and the accumulation of the heavy ion velocity distribution is started for the next scan sequence.

PHA Events:

- Two PHA events for each of the 64 data recording steps in a scan
  During the non-zero dwell time at each voltage step, the EPPS software selects two non-proton

PHA events to be reported in the FIPS telemetry. The maximum number of PHA events saved during one 64-step scan is 128.

The total number of saved PHA events saved at each stage of a scan is limited to 2*n (where n is the step number). PHA events reported in the FIPS high priority or medium priority telemetry packets have the format:

Step# (0-63)	TOF (10 MSBs)	X	Y

Where X is computed as [128*(w + (w-z)/5)/sum] MOD 64
and Y is computed as [128*(s + (s-z)/5)/sum] MOD 64

w = wedge – wedge-offset
s = strip – strip-offset
z = 14*(zigzag – zigzag-offset)/10 and sum = w+s+z

The step number, TOF value as well as the X and Y values are each stored within a 16-bit word. The required storage space for these PHA events is therefore 8*2*64 = 1024 bytes.

PHA events reported in the low priority FIPS telemetry packets have the format:

Step# (0 – 63)	Wedge	Strip	Zigzag	TOF

Each of these items is stored as a 16-bit word. Only non-proton PHA events that have not been placed into the high or medium priority telemetry packets are placed into the low priority packet to avoid duplicates.

The required storage space for these PHA events is therefore 10*2*64 = 1280 bytes.

Rate Counters:

Four Rate Channels (recorded at each step within each scan)

REFERENCES

Anger, H. O., *Instr. Soc. Am Trans. 5*, 311, 1966.

Bida, T.A., Killen, R.M., and Morgan, T.H., Discovery of calcium in Mercury's atmosphere, *Nature, 404,* 159-161, 2000.

Broadfoot, A. L., Shemansky D. E. and Kumar, S., Mariner 10: Mercury atmosphere", *Geophys. Res. Lett. 3*, pp. 577-580, 1976.

Gloeckler G. and Hsieh K.C., Time-of-flight technique for particle identification at energies from 2-400 keV/nucleon. *Nucl. Instum. Meth.* **165**, 537-544, 1979.

Gloeckler G., Ion composition measurement techniques for space plasmas. *Rev. Sci. Instrum.* **61**, 3613-3620, 1990.

Harmon, J. K., P. J. Perillat, and M. A. Slade, High-resolution radar imaging of Mercury's north pole, *Icarus, 149(2),* 1-15, 2001.

Hsieh, K. C. and E. Keppler, Extreme ultraviolet induced forward photoemission from thin carbon foils, J. Appl. Phys. 51, 2242-2246, 1980.

Hunten, D. M., Morgan, T. H. and Shemansky, D. E., The Atmosphere of Mercury, in *Mercury*, (Eds. Vilas, F., Chapman, C. R. and Matthews, M. S.), pp.562-612, University of Arizona Press, Tucson, 1988.

Ip, W.H., On solar radiation driven surface transport of sodium atoms at Mercury, *Ap. J.*, 356, 675-681, 1990.

Jursa, A. S., *Handbook of geophysics and the space environment, 4th edition*, United States Air Force, 1985.

Kabin K., Gombosi T. I. DeZeeuw D. L. and Powell K. G., Interaction of Mercury with the solar wind. *Icarus 143*, 397-406, 2000.

Knoll, G.F., *Radiation Detection and Measurement, Third Ed.,* John Wiley and Sons, New York, 2000.

Koehn, P. L., The development and testing of the Fast Imaging Plasma Spectrometer and its application in the plasma environment at Mercury, PhD Thesis, University of Michigan, Ann Arbor, Michigan, 2002.

Koehn, P. L., T. H. Zurbuchen, G. Gloeckler, R. A. Lundgren, and L. A. Fisk Measuring the plasma environment at Mercury: The Fast Imaging Plasma Spectrometer, *Meteor. and Planet. Sci.*, *37*, 1173-1190, 2002.

Ness, N.F., Behannon, K.W., Lepping, R.P., Whang, Y.C., Schatten, K.H., Magnetic field observations near Mercury: preliminary results from Mariner 10. *Science 185*, 151, 1974.

Ness, N.F., Behannon, K.W., Lepping, R.P., The magnetic field of Mercury. *J. Geophys. Res. 80,* 2708, 1975.

Potter, A. E., Killen, R., Morgan, T. H., Rapid changes in the sodium exosphere of Mercury, *Planet. Space Sci., 47*, 1441-1448, 1999.

Potter, A. E. and Morgan, T. H., Discovery of sodium in the atmosphere of Mercury, *Science, 229*, 651-653, 1985.

Potter, A. E. and Morgan, T. H., Potassium in the atmosphere of Mercury, *Icarus, 67,* 336-340, 1986.

Potter, A. E. and Morgan, T. H., Variation of sodium on Mercury with solar radiation pressure, *Icarus, 71,* 472-477, 1987.

Schwenn R., Large-scale structure of the interplanetary medium. In *Physics of the Inner Heliosphere I* (Eds. Schwenn R. and Marsch E.), pp. 99-171. Springer, Berlin, Germany, 1990.

Slade, M. A., B. J. Butler and D. O. Muhleman, Mercury radar imaging: Evidence for polar ice, *Science, 258*, 635-640, 1992.

Sprague, A. L., D. M. Hunten and K. Loders, Sulfur at Mercury: Elemental at the poles and sulfides in the regolith, *Icarus, 118*, 211-215, 1995.

Vasavada, A. R., D. A. Paige, and S. E. Wood, Near-surface temperatures on Mercury and the moon and the stability of polar ice deposits, *Icarus, 141*, 179-193, 1999.

Zurbuchen T. H., Gloeckler G., Cain J. C., Lasley S. E. and Shanks W., A low-weight plasma instrument to be used in the inner heliosphere. *SPIE Conference Proceedings, Missions to the Sun II* pp. 217-224. International Society for Optical Engineering, 1998.

Zurbuchen, T. H., P. Koehn, L. A. Fisk, T. Gombosi, G. Gloeckler, K. Kabin, On the space environment of Mercury, *,Adv. Space Res., 33*, 1884-1889, 2004.

FSCM NO.	SIZE	DRAWING NO.	REV.
88898	A	7384-9472	A
SCALE	DO NOT SCALE PRINT	SHEET 42 of 42	